



Defence Research and
Development Canada

Recherche et développement
pour la défense Canada



Extreme Agility Micro Aerial Vehicle - Control of hovering maneuvers for a mini-aerial vehicle with an onboard autopilot system

*P.-R. Bilodeau
AEREX Avionique inc.*

*F.C. Wong
DRDC Valcartier*

Defence R&D Canada – Valcartier
Technical Report
DRDC Valcartier TR 2010-144
February 2011

Canada

Extreme Agility Micro Aerial Vehicle - Control of hovering maneuvers for a mini-aerial vehicle with an onboard autopilot system

P.-R. Bilodeau
AEREX Avionique inc.

F.C. Wong
DRDC Valcartier

Defence R&D Canada – Valcartier
Technical Report
DRDC Valcartier TR 2010-144
February 2011

Principal Author

Pierre-Richard Bilodeau, Franklin Wong

Approved by

M. Lauzon
Head/Precision Weapons Section

Approved for release by

C. Carrier
Head/Document Review Panel

© Her Majesty the Queen in Right of Canada as represented by the Minister of National Defence, 2011

© Sa Majesté la Reine (en droit du Canada), telle que représentée par le ministre de la Défense nationale, 2011

Abstract

Mini Aerial Vehicles (MiniAV) are involved in various unmanned missions for both civil and military applications. These airplanes benefit from high maneuverability and can generally execute hovering and other acrobatic maneuvers. The small size of these vehicles, combined with their high maneuverability, have inspired numerous research studies in which these vehicles are envisioned for use in missions involving hazardous locations or situations in which human lives are at risk. The theoretical basis for measuring the attitude and altitude, and stabilizing a mini-aerial vehicle while being flown in a hovering position is presented. A cascaded PI control architecture based on quaternion attitude measurements and a PID altitude/throttle controller with anticipation due to aileron perturbations were formulated and implemented on an onboard autopilot. The implementation of the controllers on the onboard autopilot reduced system delays observed from an off board controller implementation from 0.17 s to 0.05 s. The result was a significant increase in the gain margin from roughly 6 to 17 dB in the pitch and yaw axes. The experimental data showed that throttle commands, compensated for aileron effects through an anticipation function, reduced the altitude hold error from ± 25 cm to ± 10 cm, thereby validating the necessity of a roll-throttle decoupler to stably hover an aircraft of this type at a fixed altitude.

Résumé

Les véhicules aériens miniatures (MiniAV) participent à diverses missions sans pilote pour des applications civiles et militaires. Ces avions possèdent d'une manœuvrabilité élevée et peuvent en général exécuter des manœuvres de vol stationnaire et d'autres manœuvres acrobatiques. La petite taille de ces véhicules, combinée à leur manœuvrabilité élevée, ont inspiré de nombreuses études, notamment pour des missions dans des endroits dangereux ou dans des situations où des vies humaines sont en danger. La base théorique de mesure de l'attitude et de l'altitude, et la stabilisation d'un véhicule aérien miniature pendant le vol stationnaire est présentée. Une architecture de cascade PI de contrôle basée sur des mesures de l'attitude en quaternion et un contrôleur de l'altitude/throttle PID avec anticipation due à des perturbations d'aileron ont été formulés et implémentés sur un autopilote à bord. La mise en oeuvre des contrôleurs sur le pilote automatique à bord réduit les retards précédents de 0,17 s à 0,05 s. Le résultat était une augmentation significative de la marge d'amplitude, passant d'environ 6 à 17 dB dans les axes de tangage et de lacet. Les données expérimentales ont montré que les commandes d'accélérateur ont compensé les effets des ailerons par une fonction d'anticipation, réduit l'erreur de tenue d'altitude à partir de ± 25 cm à ± 10 cm, validant ainsi la nécessité d'un déploiement découpleur papillon des gaz pour faire planer un avion de ce type stable et à une altitude fixe.

This page intentionally left blank.

Executive summary

Extreme Agility Micro Aerial Vehicle - Control of hovering maneuvers for a mini-aerial vehicle with an onboard autopilot system

P.-R. Bilodeau, F.C. Wong; DRDC Valcartier TR 2010-144; Defence R&D Canada – Valcartier; February 2011.

Mini Aircraft Vehicles (MiniAV) are involved in various unmanned missions for both civil and military applications. According to UAV classification, the proposed acronym MiniAV can refer to small airplanes which have a wing span of less than one meter and a weight less than five hundred grams. These airplanes benefit from high maneuverability and can generally execute hovering and other acrobatic maneuvers. The small size of these vehicles, combined with their high maneuverability, have inspired numerous research studies in which these vehicles are envisioned for use in missions involving hazardous locations or situations in which human lives are at risk. Typical applications involve inspection of collapsed buildings, structural inspection of bridges and reconnaissance for soldiers in urban scenarios.

The MiniAV in this study is a mini-fixed wing aerial vehicle which has an unstable behavior that makes manually hovering difficult for an inexperienced pilot. The implementation of an automated hovering control strategy is thus necessary if a MiniAV is to be useful for a mission specialist whose main purpose is to inspect or search a building rather than to fly the MiniAV.

In this report, the culmination of the effort to implement an onboard autopilot running a control law capable of hovering a MiniAV for the Extreme Agility Micro Aerial Vehicle Applied Research Project is presented. The theoretical basis for measuring the attitude and altitude, and stabilizing a mini-aerial vehicle while being flown in a hovering position is developed. A cascaded PI control architecture based on quaternion attitude measurements and a PID altitude/throttle controller with anticipation due to aileron perturbations were formulated and implemented on an onboard autopilot. A complementary filter was employed to improve the stability and reliability of the attitude measurements that fed the controllers. Tuning of the attitude and altitude/throttle control gains was first accomplished on a calibrated dynamic airplane model using a frequency response method to meet the desired performance goals. The calculated gains did not change significantly when implemented in the test vehicle, indicating that the airplane model dynamics were identified with good fidelity. The implementation of the controllers on the onboard autopilot reduced system delays from an off board controller implementation from 0.17 s to 0.05 s. The result was a significant increase in the gain margin from roughly 6 to 17 dB in the pitch

and yaw axes. This increase in margin means that the controller is able to handle greater model gain uncertainties and to better reduce oscillations if the vehicle is perturbed from its equilibrium position. The experimental data showed that throttle commands, compensated for aileron effects through an anticipation function, reduced the altitude hold error from ± 25 cm to ± 10 cm, thereby validating the necessity of a roll-throttle decoupler to stably hover an aircraft of this type at a fixed altitude.

Sommaire

Extreme Agility Micro Aerial Vehicle - Control of hovering maneuvers for a mini-aerial vehicle with an onboard autopilot system

P.-R. Bilodeau, F.C. Wong ; DRDC Valcartier TR 2010-144 ; R & D pour la défense Canada – Valcartier ; février 2011.

Les véhicules aériens miniature (MiniAV) participent à diverses missions sans pilote pour des applications civiles et militaires. Selon la classification des véhicules aériens inhabités (UAV), l'acronyme proposé peut référer aux avions de petite taille qui ont une envergure de moins d'un mètre et un poids de moins de cinq cents grammes. Ces avions bénéficient d'une grande manoeuvrabilité et peuvent effectuer le vol stationnaire et d'autres manoeuvres acrobatiques. La petite taille de ces véhicules et leur manoeuvrabilité ont inspiré des nombreuses études où ces véhicules sont utilisés dans des missions impliquant des lieux ou des situations dangereuses. Parmi les applications typiques figurent l'inspection des bâtiments écoulés, l'inspection structurelle des ponts et la reconnaissance des soldats dans les opérations urbaines.

Le MiniAV dans cette étude est un avion à aile fixe avec un comportement instable qui empêche un pilote sans expérience de bien le contrôler en vol stationnaire. L'implémentation d'une stratégie de contrôle pour automatiser le vol stationnaire est nécessaire si le MiniAV devient utile pour une spécialiste en mission qui a la tâche d'inspecter ou de chercher un bâtiment plutôt que de faire voler le MiniAV.

Dans ce rapport, l'aboutissement des efforts déployés pour mettre en oeuvre un autopilote à bord en cours qui exécute une loi de contrôle capable de vol stationnaire MiniAV pour le projet de recherche appliquée 'Extrême Agility Micro Aerial Vehicle' est présenté. La base théorique pour mesurer l'attitude et l'altitude, et la stabilisation du MiniAV lorsqu'il est en vol stationnaire est développée. Une architecture de contrôle proportionnelle-intégrale (PI) en cascade basée sur des mesures de l'attitude quaternion et un contrôleur proportionnelle-intégrale-dérivée (PID) pour l'altitude/accélérateur avec anticipation due aux perturbations des ailerons ont été formulés et implantés sur un autopilote à bord l'avion. Un filtre complémentaire a été employé afin d'améliorer la stabilité et la fiabilité des mesures d'attitude qui ont alimenté les contrôleurs. Le réglage des gains pour les contrôleurs de l'attitude et de l'altitude/accélérateur ont été accomplis premièrement avec un modèle dynamique et étalonné en utilisant la méthode de fréquence pour obtenir les comportements désirés. Les gains calculés n'ont pas changé significativement quand ils ont été implantés dans le véhicule de test, ce qui signifie que la dynamique a été identifiée avec une bonne fidelité. L'implémentation des contrôleurs dans l'autopilote a réduit les délais précédents de 0,17 s à

0,05 s. Le résultat a été une augmentation appréciable de la marge d'amplitude de 6 à 17 dB dans les axes de tangage et de lacet. Cette augmentation en marge permet au contrôleur de gérer les plus grandes incertitudes dans les gains et réduit plus rapidement les oscillations si le véhicule est perturbé de sa position d'équilibre. Les données expérimentales ont montré que les commandes d'accélérateur qui ont été compensées pour les effets des ailerons par une fonction d'anticipation, a réduit l'erreur en altitude constante de ± 25 cm à ± 10 cm et a permis de valider la nécessité d'avoir une découplage entre le roulis et l'accélérateur pour voler en altitude constante de façon stable et stationnaire avec ce type d'avion.

Table of contents

Abstract	i
Résumé	i
Executive summary	iii
Sommaire	v
Table of contents	vii
List of figures	x
List of tables	xiii
Nomenclature	xiv
1 Introduction	1
2 Theory	3
2.1 Reference Frames	3
2.2 Selected Attitude Representation : The Quaternion	4
2.2.1 Quaternion Defined	4
2.2.2 Multiplication Defined	5
2.2.3 The Complex Conjugate Defined	5
2.2.4 The Norm Defined	5
2.2.5 The Inverse Defined	5
2.2.6 Operator Sequences Defined	6
2.2.7 Kinematic Equation Defined	7
2.2.8 Conversion to Euler Angles	7
2.3 Attitude Estimation (Complementary Filter)	8
2.3.1 Attitude Filter Architecture	8
2.3.2 Filter Tuning	9

2.4	Comparing Quaternions from the Vision System and from the Complementary Filter	10
2.5	Attitude Control	11
2.5.1	Control Inputs of a Fixed Wing Aircraft	11
2.5.2	Attitude Output : Error quaternion	11
2.5.3	Attitude Setpoint Generation	13
2.5.4	General Architecture	14
2.5.5	Tuning	14
2.6	Altitude/Throttle Control	15
2.6.1	Architecture	15
2.6.2	Tuning	16
3	Hardware	18
3.1	Airframe	18
3.2	Autopilot	18
3.3	Additional Sensors	20
3.3.1	Vision System	20
3.3.2	Sonar Range-Finder	20
4	Sensor Data Filtering	25
4.1	Attitude Filter Algorithm Implementation	25
4.2	Tuning	25
4.3	Comparison of the Filter Outputs with a Vision System	25
5	Aircraft Model Identification	27
5.0.1	Attitude Model	27
5.0.2	Altitude Model	27

6	Control Tuning	34
6.1	Attitude Control Tuning	34
6.2	Altitude/Throttle Control Tuning	36
7	Experimental Validation of the Tuned Controllers	38
7.1	Attitude Control Results	38
7.2	Altitude/Throttle Stabilization Results	44
7.3	Effect of the Throttle on the Roll Controller	45
8	Conclusions	47
9	Recommendations	48
	References	49
	Annex A: User Guide	51

List of figures

Figure 1:	Reference frames definition (top view)	3
Figure 2:	Rotation operator composition $L_q \circ L_p$	6
Figure 3:	Complementary filter based on the quaternion formulation	9
Figure 4:	Vision system and autopilot reference frames definitions	11
Figure 5:	Control inputs of a fixed wing	12
Figure 6:	Error quaternion	13
Figure 7:	Representative attitude control architecture	14
Figure 8:	Acceptable response limits for unstable, integrator and stable processes	15
Figure 9:	Altitude control architecture	16
Figure 10:	Typical frequency response of the closed loop altitude system . . .	17
Figure 11:	Flatana from Great Planes	18
Figure 12:	Procerus Kestrel 2.22 (www.procerusuav.com)	19
Figure 13:	Communication box (www.procerusuav.com)	19
Figure 14:	Vision reference frame relative to the calibration square	20
Figure 15:	Maxbotix MaxSonar EZ serie (www.maxbotix.com)	21
Figure 16:	Beam patterns of the MaxSonar EZ serie (www.maxbotix.com) . .	21
Figure 17:	Response of the range-finder MaxSonar EZ0	22
Figure 18:	Response of the range-finder MaxSonar EZ2	22
Figure 19:	Response of the range-finder MaxSonar EZ4	23
Figure 20:	Comparison between the sonar and the vision system outputs . . .	24
Figure 21:	Comparison between the outputs of the attitude estimator without magnetometers and of a vision system : – fusion, — vision	26

Figure 22: Fit for the open loop identification of the coupling between $\delta_{throttle}$ and the altitude. Dashed line - fit. Solid - measured. Relative to operation points.	28
Figure 23: Validation fit for the open loop identification of the coupling between $\delta_{throttle}$ and the altitude. Dashed line - fit. Solid - measured. Relative to operation points.	29
Figure 24: Autocorrelation of residuals for the coupling between the altitude and $\delta_{throttle}$	30
Figure 25: Fit for the open loop identification of the coupling between $\delta_{aileron}$ s and the altitude. Dashed line - fit. Solid - measured. Relative to operation points.	31
Figure 26: Validation fit for the open loop identification of the coupling between $\delta_{aileron}$ s and the altitude. Dashed line - fit. Solid - measured. Relative to operation points.	32
Figure 27: Autocorrelation of residuals for the coupling between the altitude and $\delta_{aileron}$ s	33
Figure 28: Frequency response of the attitude controllers with different time delays	35
Figure 29: Frequency response of the altitude controller	36
Figure 30: Step response of the coupling between $\delta_{aileron}$ s and h	37
Figure 31: Flight results #1 obtained with the Flatana	40
Figure 32: Flight results #2 obtained with the Flatana	41
Figure 33: Flight results #3 obtained with the Flatana	42
Figure 34: Flight results #4 obtained with the Flatana	43
Figure 35: Flight results with altitude controller : ± 0.25 cm bounds	44
Figure 36: Flight results with altitude controller and static decoupler : ± 0.10 cm bounds	45
Figure 37: Flight results #3 - Effect of throttle variation on the roll controller	46
Figure A.1: Joystick and switch configurations on the controller handset	51

List of tables

Table 1:	Rotation sequence orders	7
Table 2:	Input variable nomenclature	11
Table 3:	Input conversion gains (ms to deg and %)	12
Table 4:	Outside characteristics of the tested sonar range-finders	23
Table 5:	Identified transfer functions for the altitude	33
Table 6:	Controller parameters	34
Table 7:	Property of the closed loop system with the 0.17 s and 0.05 s time delay	36

Nomenclature

δ	Manipulated variables vector, $[\delta_{\text{ailerons}}, \delta_{\text{elevator}}, \delta_{\text{rudder}}]'$, ms
δ_{ailerons}	Ailerons deflection, ms
δ_{elevator}	Elevator deflection, ms
δ_{rudder}	Rudder deflection, ms
δ_{throttle}	Throttle command, ms
ϕ	Angle in roll, rad
θ	Angle in pitch, rad
ψ	Angle in yaw, rad
ω_{co}	Crossover frequency, rad/s
q	Quaternion, $[q_w, q_x, q_y, q_z]'$
\dot{q}	Quaternion derivative, $[\dot{q}_w, \dot{q}_x, \dot{q}_y, \dot{q}_z]'$
q^d	Desired quaternion, $[q_w^d, q_x^d, q_y^d, q_z^d]'$
q^e	Error quaternion, $[q_w^e, q_x^e, q_y^e, q_z^e]'$
q^m	Measured quaternion, $[q_w^m, q_x^m, q_y^m, q_z^m]'$
q^v	Vertical quaternion, $[0.7071, 0, 0.7071, 0]'$
Θ	Error between the desired and measured attitude expressed in Euler angles $[\phi, \theta, \psi]'$, rad
Ω	Angular rates, $[\omega_x, \omega_y, \omega_z]'$, rad/s
ϕ_m	Phase margin, deg
ω_x	Roll rate, rad/s
ω_y	Pitch rate, rad/s
ω_z	Yaw rate, rad/s
A_m	Amplitude margin, dB
\mathbf{G}_c	Attitude regulator, $\text{diag}(G_{c_\phi}, G_{c_\theta}, G_{c_\psi})$
$G_{\omega_x}(s)$	Transfer function between the ailerons deflection and the roll rate
$G_{\omega_y}(s)$	Transfer function between the elevator deflection and the pitch rate
$G_{\omega_z}(s)$	Transfer function between the rudder deflection and yaw rate
$G_\phi(s)$	Transfer function between the ailerons deflection and the roll error
$G_\theta(s)$	Transfer function between the elevator deflection and the pitch error
$G_\psi(s)$	Transfer function between the rudder deflection and the yaw error
\mathbf{K}	Internal proportional gains, $\text{diag}(K_p, K_q, K_r)$
M_r	Maximum peak resonance, dB
PID	Proportional-Integrator-Derivative Regulator
s	Laplace operator
<i>Subscript</i>	
B	Body axis
E	NED axis

Superscript

cmd Deflection command generated by the controller
trim Trim value of the surface deflection

This page intentionally left blank.

1 Introduction

Mini Aerial Vehicles (MiniAV) are involved in various unmanned missions for both civil and military applications. According to the classification given by Mueller and al. (2007), the proposed acronym MiniAV can refer to small airplanes which have a wing span of less than one meter and a weight of less than five hundred grams. The small size of these vehicles, combined with their high maneuverability, have inspired numerous research studies in which these vehicles are envisioned for use in missions involving hazardous locations or situations in which human lives are at risk. Typical applications involve inspection of collapsed buildings, structural inspection of bridges and reconnaissance for soldiers in urban scenarios.

There are three essential criteria for any man-carried airborne sensor: 1) it must be able to fly at very low forward speed, 2) it must be structurally robust, and 3) it must be able to fly by itself. To address the first two points, several types of MAVs have been developed in the past. Fixed-wing designs are structurally robust but they cannot fly at very slow forward speeds in standard attitudes. Rotorcraft designs can fly slowly except their mechanical control system is not structurally robust in comparison to a fixed-wing design. An alternative to these two types of platforms is a platform that is capable of hybrid mode flight. For example, if a high performance lightweight fixed-wing MAV can be commanded to execute fast level flight or to execute a maneuver known as 'prop hanging' or 'hovering' for slow forward flight, the characteristics of structural robustness and slow flight may be obtained with a fixed-wing design. Manually piloting a fixed-wing MAV to hover for an extended length of time takes great concentration and skill. If the hovering maneuver can be automated, then it is possible to create a robust, slow flying airborne sensor that a soldier can use with little effort.

A structured approach for developing and implementing controllers generally involves mathematical models of the system to be controlled. This topic was covered by Bilodeau (2009) for a vehicle that used an offboard controller. In this study, which is a sequel to Bilodeau (2009)'s work, an onboard control system is implemented on the vehicle.

In the literature, several authors proposed a systematic approach to design fixed wing control strategies for hovering based on an identified model composed of linear transfer functions. Green and Oh (2005, 2006a,b) and Green (2007) suggested standard proportional-integral-derivative (PID) controllers based on quaternion attitude representation. To adjust controller parameters, the authors used an empirical and iterative method. Satisfactory results were obtained with a commercial inertial measurement unit (IMU) and an airframe similar to the one discussed in this report. However, a major difference compared to the present work is that Green added extra motors to the wing tips to improve the control authority of the system.

Knoebel et al. (2006), Knoebel (2007), Knoebel and Mc Lain (2008) compared non-adaptive regulators with gain scheduling based on the main air stream speed with more sophisticated adaptive regulators. The proposed non-adaptive regulators base structure is very similar to the one studied. Mechanical parameters were estimated with thin airfoil theory (Phillips (2004)). Adequate performance was reached for a miniature tail-sitter airframe. Frank et al. (2007) presented a theoretical modeling method where the parameters were obtained by estimation. DeBlauwe et al. (2007) identified a first order model based on force and moment equations. This approach required a measurement or an accurate estimation of the translational speed. Such information was difficult to obtain with low cost sensors. For hovering control, both authors, Frank and De Blauwe, proposed full state feedback regulators tuned with linear quadratic techniques for a MiniAV airframe. However, they used an external vision system to obtain feedback variables. Finally, Stone (2004) determined a model of a fuel engine tail sitter with a system identification approach. LQR and PID controllers were designed. While Stone's airframe is too large for our envisioned indoor operations, the modeling approach was retained for identifying the airframe in Bilodeau (2009).

This report documents the implementation of an onboard autopilot and control law that allows a mini-aerial vehicle to execute a stable hovering maneuver. The work was sponsored under the DRDC Partner Group 2, Sense Thrust Advisory Group, applied research project entitled 'Extreme agility micro-aerial vehicle concepts for complex terrain warfare' between 2007 and 2009. The information provided is a culmination of the effort carried out in the work breakdown element 'Flight Control'.

The objective of this report is to present the performance obtained with a complete control system mounted onboard the MiniAV rather than the hybrid onboard wireless inertial measurement unit and offboard controller previously used by Bilodeau (2009). As a secondary objective, the report will demonstrate that simple sensor fusion algorithms can estimate correctly the attitude of a hovering air vehicle. The report is separated as follows. A theoretical overview of the reference frame definitions, quaternion representation, complementary filter, and controller architecture and tuning method is given. Then, the testbed used to produce the results is presented. The fusion filter implementation is assessed and is followed by a presentation of the MiniAV model used for control tuning. Finally, experimental validation results of the model and controllers are presented.

2 Theory

This chapter presents the theoretical basis of the reference frames, quaternion attitude representation, and the attitude estimation filter (complementary filter). A description of the control inputs is provided. Finally, the control theory for the complete attitude regulation is presented.

2.1 Reference Frames

There are two main reference frames used in this document. The first is an inertial reference frame denoted as R_E and defined as the North-East-Down (NED) reference frame. The earth axes, X_E , Y_E and Z_E , are oriented toward north, east and down, respectively. The second reference frame is the body axis reference frame denoted as R_B and is attached to the body of the air vehicle as illustrated in Figure 1. Also, the origin of the body axes is located at the vehicle's center of mass. The X_B , Y_B and Z_B axes point toward the front, right and ventral side of the air vehicle, respectively.

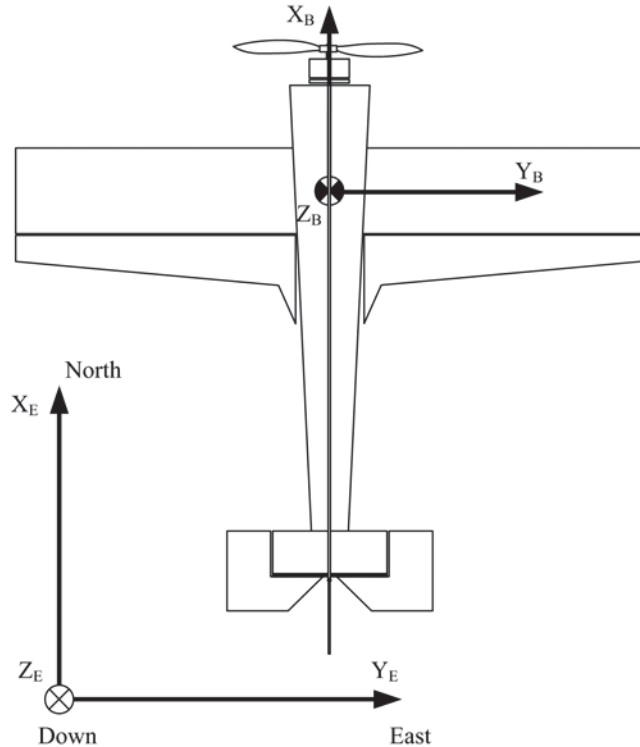


Figure 1: Reference frames definition (top view)

2.2 Selected Attitude Representation : The Quaternion

Phillips et al. (2001) made a review of the popular attitude representations used for aircraft kinematics. The authors presented the well-known Euler angles, Euler-axis rotation parameters, direction cosines and Euler-Rodrigues quaternion. From the authors' conclusions, the quaternion is by far superior to the other attitude representations based on the computational cost alone. Also, the quaternion can represent any orientation without the singularity problem that Euler angles encounter when orientations of $\pm 90^\circ$ occur. The direction cosine does not possess singularities but it takes more computational power because there are nine elements to integrate versus four for quaternions. Thus, the quaternion was selected for the implementation of the attitude estimator and of the attitude controllers even though they are less intuitive in their interpretation.

This section presents a summary of quaternion properties used for implementation of the control algorithms. For a more detailed description of quaternion properties, see Kuipers (1999).

2.2.1 Quaternion Defined

In what follows, a quaternion will always be denoted by a lower-case letter, say p or q or r . Bold-faced letters are used to denote ordinary vectors in three dimensional space, namely R^3 . To denote the standard orthonormal basis, \mathbf{i} , \mathbf{j} and \mathbf{k} are used and these vectors are written as

$$\begin{aligned}\mathbf{i} &= (1, 0, 0) \\ \mathbf{j} &= (0, 1, 0) \\ \mathbf{k} &= (0, 0, 1)\end{aligned}$$

A quaternion is composed of four real numbers or scalars and can be written as

$$q = (q_w, q_x, q_y, q_z)$$

To better understand the nature of the quaternion, an alternative way of representing it is to first define a scalar part, say q_w . Then, a vector part, say \mathbf{q} , which is a vector defined in R^3 as

$$\mathbf{q} = \mathbf{i}q_x + \mathbf{j}q_y + \mathbf{k}q_z$$

where \mathbf{i} , \mathbf{j} and \mathbf{k} are the standard orthonormal basis in R^3 . Now, the quaternion can be defined as the sum

$$q = q_w + \mathbf{q}$$

where q_w is the scalar part and \mathbf{q} is the vector part of the quaternion.

2.2.2 Multiplication Defined

Let the definition of the product of two quaternions, p and q , be $r = pq \cdot pq$. pq can be written in the following form

$$pq = p_w q_w - \mathbf{p} \cdot \mathbf{q} + p_w \mathbf{q} + q_w \mathbf{p} + \mathbf{p} \times \mathbf{q}$$

which can be expand in the following form

$$\begin{aligned} r_w &= p_w q_w - p_x q_x - p_y q_y - p_z q_z \\ r_x &= p_x q_w + p_w q_x - p_z q_y + p_y q_z \\ r_y &= p_y q_w + p_z q_x + p_w q_y - p_x q_z \\ r_z &= p_z q_w - p_y q_x + p_x q_y + p_w q_z \end{aligned}$$

or if written in matrix notation

$$\begin{bmatrix} r_w \\ r_x \\ r_y \\ r_z \end{bmatrix} = \begin{bmatrix} p_w & -p_x & -p_y & -p_z \\ p_x & p_w & -p_z & p_y \\ p_y & p_z & p_w & -p_x \\ p_z & -p_y & p_x & p_w \end{bmatrix} \begin{bmatrix} q_w \\ q_x \\ q_y \\ q_z \end{bmatrix} \quad (1)$$

2.2.3 The Complex Conjugate Defined

The complex conjugate of the quaternion $q = q_w + \mathbf{q} = q_w + \mathbf{i}q_x + \mathbf{j}q_y + \mathbf{k}q_z$, denoted q^* , is given by

$$q^* = q_w - \mathbf{q} = q_w - \mathbf{i}q_x - \mathbf{j}q_y - \mathbf{k}q_z \quad (2)$$

When the complex conjugate is applied to a product of quaternions, the result is the product of the individual complex conjugates in a reversed order. Given any two quaternion p and q , we have

$$(pq)^* = q^* p^*$$

2.2.4 The Norm Defined

The norm of a quaternion is defined by

$$N(q) = \sqrt{q^* q} = \sqrt{q_w^2 + q_x^2 + q_y^2 + q_z^2} = |q| \quad (3)$$

Further, a unit quaternion, $N(q) = 1$, will always be assumed.

2.2.5 The Inverse Defined

As demonstrated in Kuipers (1999), specifying $N(q) = 1$ gives the following equality

$$q^{-1} = q^* \quad (4)$$

which describes the quaternion inverse q^{-1} as equal to the quaternion complex conjugate.

2.2.6 Operator Sequences Defined

The quaternion rotation operator can be used for two different applications. The first one is to apply one or many rotations to a vector, say \mathbf{u} , while keeping the same reference frame all along the operations. The second one is to change the reference frame of the vector to another frame of reference. To illustrate the difference between these two applications, let us define the vectors \mathbf{u} , \mathbf{v} and \mathbf{w} which are illustrated in Figure 2.

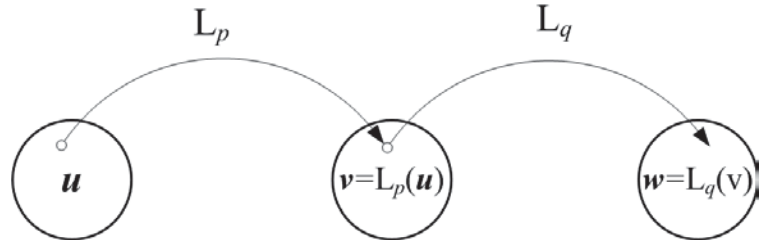


Figure 2: Rotation operator composition $L_q \circ L_p$

To express a rotation sequence of a vector \mathbf{u} to the final vector \mathbf{w} , let p and q be the unit quaternions which define the quaternion rotation operators

$$L_p(\mathbf{u}) = p\mathbf{u}p^*$$

and

$$L_q(\mathbf{v}) = q\mathbf{v}q^*$$

Therefore, \mathbf{w} can be obtained as follows

$$\begin{aligned}\mathbf{w} &= L_q(\mathbf{v}) \\ &= q\mathbf{v}q^* \\ &= q(p\mathbf{u}p^*)q^* \\ &= (qp)\mathbf{u}(qp)^* = L_{qp}\end{aligned}$$

This result means that the quaternion equal to the rotation from \mathbf{u} to \mathbf{w} is qp and can be read as the rotation p followed by the rotation q .

Now, if one wants to express \mathbf{u} in the reference frame of \mathbf{w} , the operator L_p and L_q must be redefined as follows

$$L_p(\mathbf{u}) = p^*\mathbf{u}p$$

and

$$L_q(\mathbf{v}) = q^*\mathbf{v}q$$

Therefore, to express \mathbf{u} in the reference frame where \mathbf{w} stands, one must apply the following logic

$$\begin{aligned}\mathbf{w} &= \mathbf{L}_q(\mathbf{v}) \\ &= q^* \mathbf{v} q \\ &= q^* (p^* \mathbf{u} p) q \\ &= (pq)^* \mathbf{u} (pq) = \mathbf{L}_{pq}\end{aligned}$$

This gives an equivalent rotation pq which can also be read as the rotation p followed by the rotation q .

The two rotation sequence orders are summarized in Table 1.

Table 1: Rotation sequence orders

Type of rotation	p followed by q	Rotation operator
Vector rotation	qp	$(qp)\mathbf{u}(qp)^*$
Frame rotation	pq	$(pq)^*\mathbf{u}(pq)$

2.2.7 Kinematic Equation Defined

The kinematic equation of the quaternion introduces the quaternion derivative \dot{q} and the pure quaternion, say $p(\boldsymbol{\Omega})$, expressing the body axis angular rates in a quaternion formulation where $\boldsymbol{\Omega} = [\omega_x, \omega_y, \omega_z]$. $p(\boldsymbol{\Omega})$ can be written as

$$p(\boldsymbol{\Omega}) = [0, \omega_x, \omega_y, \omega_z]^T$$

With these terms defined, the kinematic equation is given by

$$\dot{q} = \frac{1}{2} qp(\boldsymbol{\Omega})$$

2.2.8 Conversion to Euler Angles

Because the quaternion is not very intuitive and because Euler angles can be attached directly to the body axis, the Euler angles offer a better physical visualization and data interpretation. The conversion from quaternions to Euler angles are

$$\phi = \arctan\left(\frac{2(q_w q_x + q_y q_z)}{1 - 2(q_x^2 + q_y^2)}\right) \quad (5)$$

$$\theta = \arcsin \left(2(q_w q_y - q_x q_z) \right) \quad (6)$$

$$\psi = \arctan \left(\frac{2(q_x q_y + q_w q_z)}{1 - 2(q_y^2 + q_z^2)} \right) \quad (7)$$

2.3 Attitude Estimation (Complementary Filter)

In past studies, Phillips et al. (2001) reviewed popular attitude representations for aircraft kinematics. The authors examined Euler angles, Euler-axis rotation parameters, direction cosines and the Euler-Rodrigues quaternion. The authors concluded that the quaternion was by far superior to other representations based on the computational cost alone.

To improve the stability and reliability of the attitude signals feeding controllers, several authors (Yun and Bachmann (2006), Ahmadi et al. (2007)) proposed the use of Kalman filters which in practice are not very easy to implement on embedded systems. Hamel and Mahony (2006), Mahony et al. (2006), Metni et al. (2006) used a complementary filter to estimate attitudes for vertical take-off and landing (VTOL) UAVs. The attitude estimation algorithm proposed by Hamel and Mahony (2006) which is based on an explicit complementary filter is used here. Since the microcontroller has limited computational resources, the implementation of the filter is based on the quaternion representation instead of the rotation matrix implemented by Hamel and Mahony (2006).

2.3.1 Attitude Filter Architecture

The attitude filter architecture is illustrated in Figure 3 and can be separated in two parts. The first part consists of the quaternion kinematic equation $\dot{\mathbf{q}} = \frac{1}{2}qp(\boldsymbol{\Omega})$ described in subsection 2.2.7 where $\boldsymbol{\Omega}$ is the corrected angular rate vector. If no corrections are made to the rate-gyros measurements $\boldsymbol{\Omega}^y$, the rate-gyros bias will be integrated and the quaternion estimate will drift in time.

To reduce the drift in the attitude estimation, the complementary filter estimates the rate-gyros bias with inertial measurements. One can use only accelerometers readings \mathbf{a}^y or in combination with flux-magnetometers readings \mathbf{m}^y to improve the estimate of the rate-gyros bias. Flux-magnetometers were not retained here because the hardware employed in this project did not possess a tri-axis magnetometer. Even if a tri-axis magnetometer was available, it is very likely that it would not give reliable measurements inside buildings due to the presence of metallic structures. This topic is discussed by Bachmann et al. (2007).

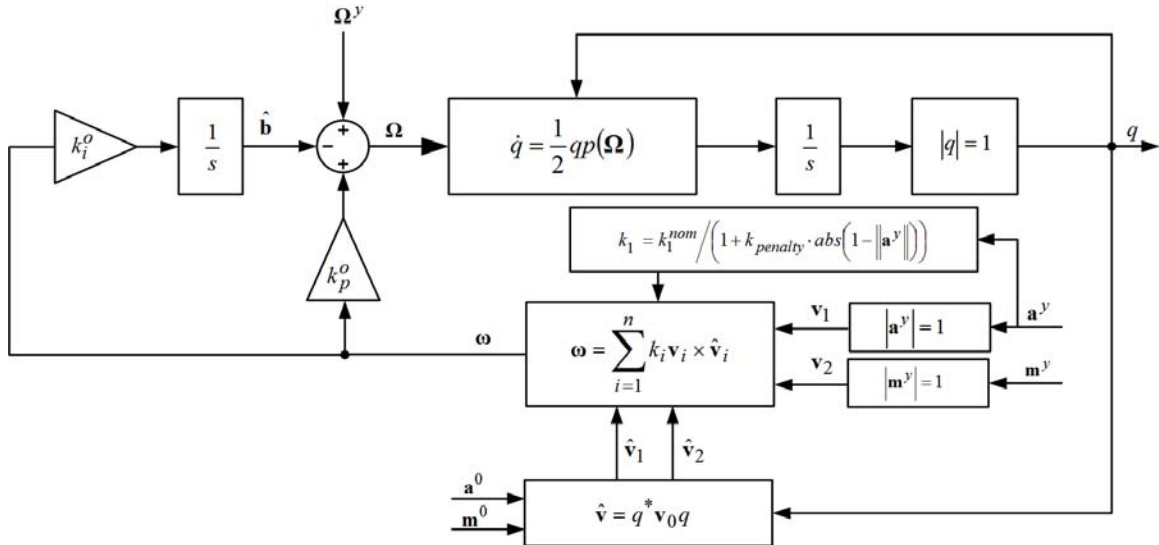


Figure 3: Complementary filter based on the quaternion formulation

To estimate the rate-gyro bias, an estimate of the inertial sensor measurements $\hat{\mathbf{v}}_i$ is first done by transposing the nominal values of the measured inertial quantities on the body axis reference frame. This is done with the equation $\hat{\mathbf{v}} = \mathbf{q}^* \mathbf{v}_0 \mathbf{q}$. Then, the estimated readings can be compared with the inertial sensors readings with the equation $\boldsymbol{\omega} = \sum_{i=1}^n k_i \mathbf{v}_i \times \hat{\mathbf{v}}_i$ where k_i is a confidence gain and n is the number of inertial sensor triads. In general, accelerometers provide low noise readings, thus a gain near 1.0 is generally retained. However, the accelerometer estimates will differ from the measurements if the body is accelerating and this will produce a perturbation on the bias estimate. To avoid this from occurring, the accelerometers confidence gain k_1 is modified as a function of the measured acceleration with a penalty gain $k_{penalty}$. The more the body is accelerating, the lower the confidence in the gravitational acceleration readings. $\boldsymbol{\omega}$ is an instantaneous improvement vector which is used directly to correct Ω^y and to estimate the rate-gyro bias through integration. Finally, the dynamics of the filter can be tuned with the parameters k_p^o and k_i^o which are the proportional and integral gains of the filter observer, respectively.

2.3.2 Filter Tuning

The classical complementary filter equation, given by Metni et al. (2006), is

$$\hat{X}(s) = \frac{s^2}{s^2 + k_p^o s + k_i^o} X_\Omega(s) + \frac{k_p^o s + k_i^o}{s^2 + k_p^o s + k_i^o} X(s) \quad (8)$$

where $\hat{X}(s)$ represents the estimated attitude, $X_\Omega(s)$ represents the estimated attitude using angular rates and $X(s)$ represents the true attitude. From equation 8, it is

possible to see that the first transfer function is a high pass filter and that the second transfer function is a low pass filter. Also, it is worth noting that the sum of these two transfer functions is equal to 1. This property is the reason why it is called a complementary filter.

The denominators of equation 8 follow the form $s^2 + 2\zeta\omega_0s + \omega_0^2$, thus the following equalities

$$k_p^o = 2\zeta\omega_0 \quad (9)$$

$$k_i^o = \omega_0^2 \quad (10)$$

can be extracted. In these equalities, ζ is the damping ratio and ω_0 is the cutoff frequency.

2.4 Comparing Quaternions from the Vision System and from the Complementary Filter

A good way to evaluate the performance of the complementary filter is to compare its attitude estimates with the attitudes measured by a vision system. Figure 4 illustrates the different reference frames encountered when using a vision system and an onboard autopilot (Kestrel, Procerus Technologies). There are four reference frames: 1) the inertial reference frame \mathcal{R}_E , 2) the vision system reference frame \mathcal{R}_V , 3) the body axis reference frame of the autopilot (Kestrel) \mathcal{R}_{Be} and, 4) the body axis reference frame of the vision system \mathcal{R}_{Bv} . The quaternions $q^{kestrel}$ and q^{vision} are known. However, the quaternions q^{V2E} , vision frame with respect to inertial frame, and q^{Bv2Be} , vision body frame with respect to inertial frame, are unknown unless measured. These unknown quaternions can be determined by minimizing the cost function if measurement is not an option as was the case here. The following cost function was used

$$\text{cost} = 0.5 * q_x^e * q_x^e + 0.5 * q_y^e * q_y^e + 0.5 * q_z^e * q_z^e;$$

where q^e is defined as

$$q^e = q^A(q^B)^{-1}$$

and where q^A and q^B are defined as

$$\begin{aligned} q^A &= q^{V2E} q^{kestrel} \\ q^B &= q^{vision} q^{Bv2Be} \end{aligned}$$

When minimizing the cost function, it is very important to apply a unitary norm constraint for both q^A and q^B . Knowing q^{V2E} and q^{Bv2Be} , it is possible to calculate the equivalent quaternion coming from the vision system to the one estimated by the complementary filter on the Kestrel autopilot. This new quaternion is named $q^{kestrel_from_vision}$ and is defined as

$$q^{kestrel_from_vision} = (q^{V2E})^{-1} q^{vision} q^{Bv2Be}$$

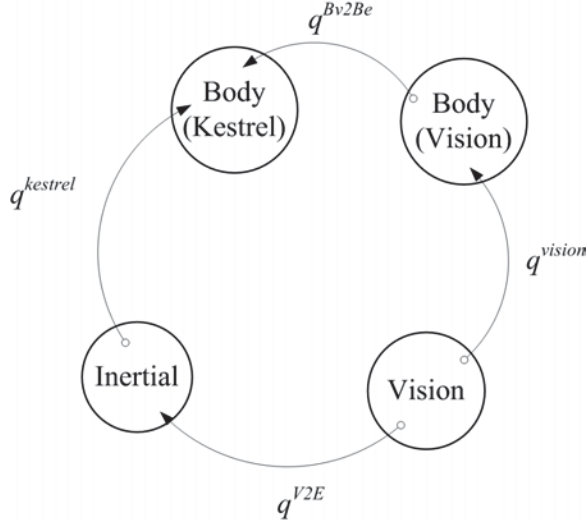


Figure 4: Vision system and autopilot reference frames definitions

2.5 Attitude Control

2.5.1 Control Inputs of a Fixed Wing Aircraft

The available control surfaces and control device (see Figure 5) are the ailerons, the elevator, the rudder and the throttle. The variables associated to these inputs are presented in Table 2 where the superscript trim represents the trim value of the associated input and where the superscript cmd represents the command value around the operating point. The units of these input variables are in milliseconds because they represent the servo commands which are pulse widths varying from 1.0 to 2.0 milliseconds. To convert these servo commands into surface deflections or percentages of the throttle, the gains presented in Table 3 can be applied.

Table 2: Input variable nomenclature

Control surface/device	Servo command (ms)	Controller/pilot command (ms)	Servo trim value (ms)
Ailerons	δ_{ailers}	δ_{ailers}^{cmd}	δ_{ailers}^{trim}
Elevator	$\delta_{elevator}$	$\delta_{elevator}^{cmd}$	$\delta_{elevator}^{trim}$
Rudder	δ_{rudder}	δ_{rudder}^{cmd}	δ_{rudder}^{trim}
Throttle	$\delta_{throttle}$	$\delta_{throttle}^{cmd}$	$\delta_{throttle}^{trim}$

2.5.2 Attitude Output : Error quaternion

The error quaternion is only involved in control and represents the difference between the actual and the desired attitude, as illustrated in Figure 6. In this figure, q^m , q^d

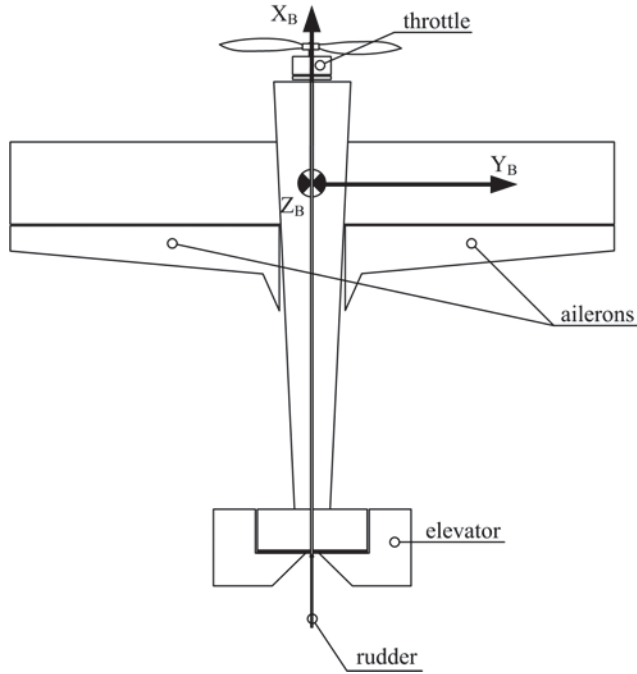


Figure 5: Control inputs of a fixed wing

Table 3: Input conversion gains (ms to deg and %)

Control surface/device	Gain (deg/ms)	Gain (%/ms))
Ailerons	111.041	n/a
Elevator	112.392	n/a
Rudder	168.493	n/a
Throttle	n/a	% = 125

and q^e , respectively, represent the measured, desired and error quaternions and the circles represent the reference frames. Therefore, q^m represents the rotation which brings R_E to R_B , q^d brings R_E to the desired reference frame R_D and q^e brings R_B to R_D .

From Figure 6, a reference frame relation can be established between q^m , q^d and q^e and take the form

$$q^d = q^m q^e$$

By isolating q^e , the equation describing the error quaternion can be found as

$$q^e = (q^m)^{-1} q^d \quad (11)$$

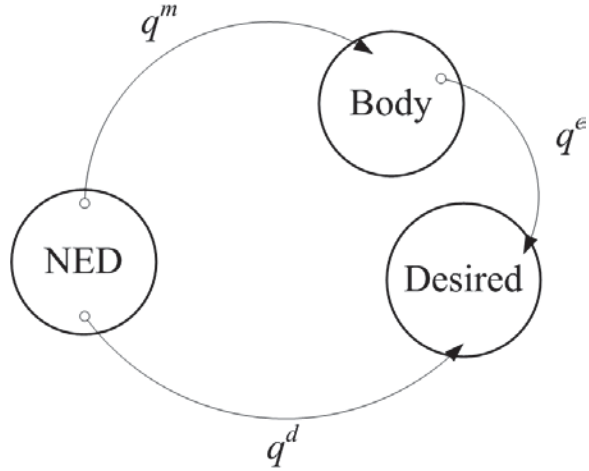


Figure 6: Error quaternion

2.5.3 Attitude Setpoint Generation

The attitude is set by the desired quaternion q^d . In hover, q^d takes the value of a vertical quaternion facing north, q^v , as defined by

$$q^v = [0.7071, 0, 0.7071, 0]'$$

To add control around the roll, pitch and yaw axis, the following quaternions are defined

$$\begin{aligned} q^{roll} &= [\cos(\bar{\phi}/2), \sin(\bar{\phi}/2), 0, 0]' \\ q^{pitch} &= [\cos(\bar{\theta}/2), 0, \sin(\bar{\theta}/2), 0]' \\ q^{yaw} &= [\cos(\bar{\psi}/2), 0, 0, \sin(\bar{\psi}/2)]' \end{aligned}$$

where $\bar{\phi}$, $\bar{\theta}$ and $\bar{\psi}$ define the roll, pitch and yaw setpoints around the vertical axis. The mathematical implementation of these quaternion is carried out by

$$q^d = q^v q^{roll} q^{pitch} q^{yaw}$$

q^v , however, is not a good vertical quaternion when the air vehicle controller is initialized with a non-zero heading because it will generate an immediate yaw correction which might temporarily destabilize the air vehicle. Therefore, to generate a vertical quaternion with the proper initial heading, a delta quaternion that represents the initial aircraft attitude to the vertical orientation is calculated as proposed by Green (2007) and used in Bilodeau (2009).

2.5.4 General Architecture

The control architecture (Bilodeau (2009)) is illustrated in Figure 7. The term \mathbf{G}_c is defined as a diagonal 3×3 matrix composed of proportional-integral (PI) regulators of the form

$$G_c = \frac{K_c(T_i s + 1)}{T_i s} \quad (12)$$

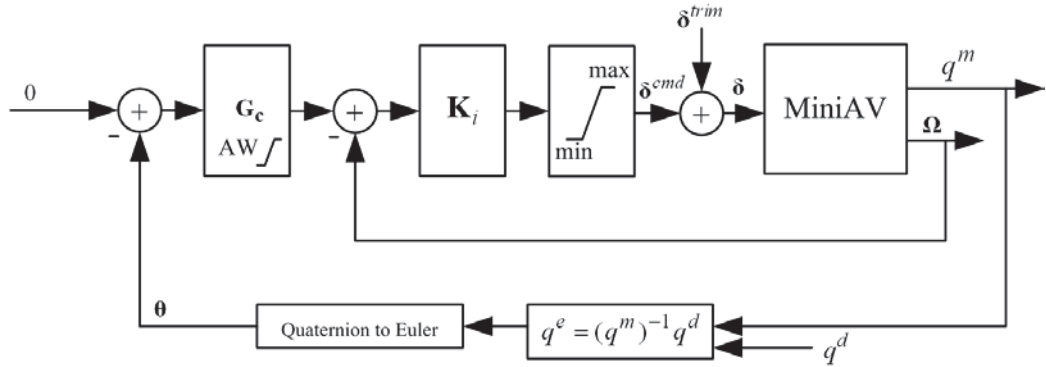


Figure 7: Representative attitude control architecture

Each PI is implemented with an anti-windup form. \mathbf{K}_i is a 3×3 diagonal matrix composed of proportional gains. q^d , q^m and q^e are the desired, measured and error quaternions, respectively. Θ and Ω are the error angle vector $[\phi, \theta, \psi]$ and the angle rate vector $[\omega_x, \omega_y, \omega_z]$. $\boldsymbol{\delta}$ is the manipulated variable vector $[\delta_{aileron}, \delta_{elevator}, \delta_{rudder}]$. $\boldsymbol{\delta}^{trim}$ and $\boldsymbol{\delta}^{cmd}$ are the trim and command vectors, respectively, associated to $\boldsymbol{\delta}$. The input $\delta_{throttle}$ is not considered in the attitude problem because it is considered as a perturbation for the roll controller.

It is worth noting that, in Bilodeau (2009), q^d was fixed equal to q^v as calculated by Green (2007)'s algorithm. It is also worth nothing that the attitude setpoints were applied on Θ rather than in q^d . While this implementation is not elegant, it allows attitude setpoints to be directly included in q^d . That is why a setpoint of zero appears in Figure 7.

2.5.5 Tuning

To determine the controller parameters, a tuning method based on frequency response was used. It relies on the contours of the Nichols chart and is described by Pomerleau and Poulin (1996) and Poulin and Pomerleau (1996). By specifying a contour which corresponds to the maximum peak resonance M_r of the closed loop transfer function, a minimum phase margin ϕ_m and a minimum gain margin A_m is specified to control the maximum peak overshoot of the system for setpoint changes.

For the cascade loop presented in Figure 7, this tuning method is applied on the external loop to follow the M_r specification. The internal gains are adjusted to accelerate or decelerate the system while providing the highest gain crossover frequency possible. The external loop is used to eliminate the static error. The maximum M_r is 3 dB which will result in a good compromise between performance, overshoot and oscillations. The minimum M_r for low frequencies is of 0 dB to ensure no static error. Finally, Figure 8 illustrates acceptable response limits for the tuning of the attitude loops and for any process stability type (stable, integrator, unstable).

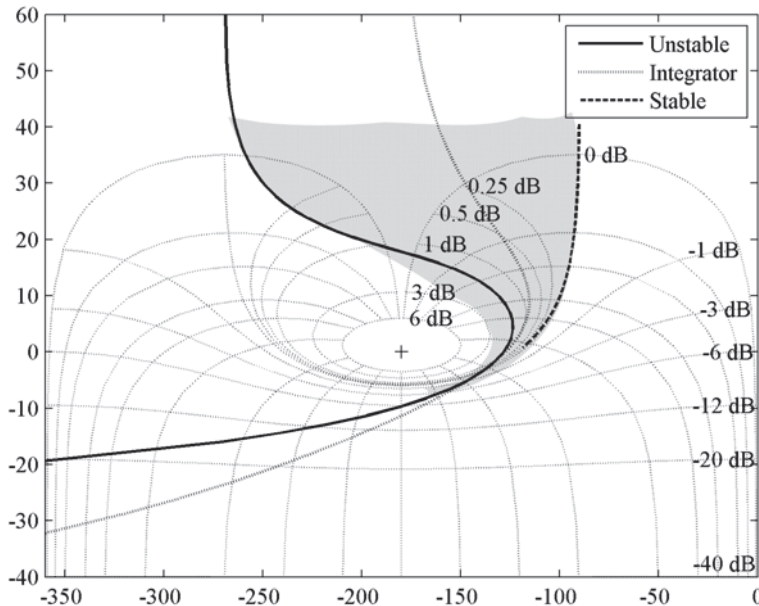


Figure 8: Acceptable response limits for unstable, integrator and stable processes

2.6 Altitude/Throttle Control

2.6.1 Architecture

The control architecture for the altitude/throttle controller is illustrated in Figure 9. It consists of a proportional-integral-derivative (PID) controller with anti-windup and an anticipation transfer function D used to counteract the coupling between the ailerons and the altitude/throttle. For the altitude measurement, a sonar range-finder is used. Its signal is filtered with an anti-peak algorithm and a low-pass filter with a time constant of 0.1 s. The anti-peak algorithm was a zero-order hold triggered when $\|\Delta h\| \geq 0.15$ m.

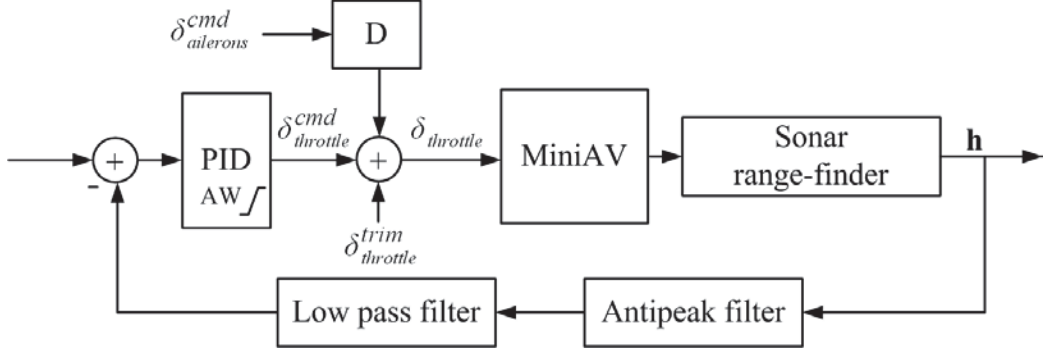


Figure 9: Altitude control architecture

The PID structure is given by

$$G_a = \frac{K_c(T_i s + 1)(T_d s + 1)}{T_i s(T_f s + 1)} \quad (13)$$

2.6.2 Tuning

The tuning method is the same than for the attitude controllers. However, to obtain a good perturbation rejection, it was observed that a very high phase advance is preferable to a high gain adjustment. Figure 10 illustrates this idea with a typical second order transfer function and an integrator pole that is similar to the altitude response observed with the actual MiniAV.

To determine D , where the aileron is considered a perturbation to the throttle controller, the following anticipation design equation is used

$$D = -\frac{G_{aileron}}{G_{throttle}} \quad (14)$$

where D , $G_{aileron}$ and $G_{throttle}$ represent, respectively, the ideal decoupler, the perturbation transfer function for the aileron command and the process transfer function for the throttle command.

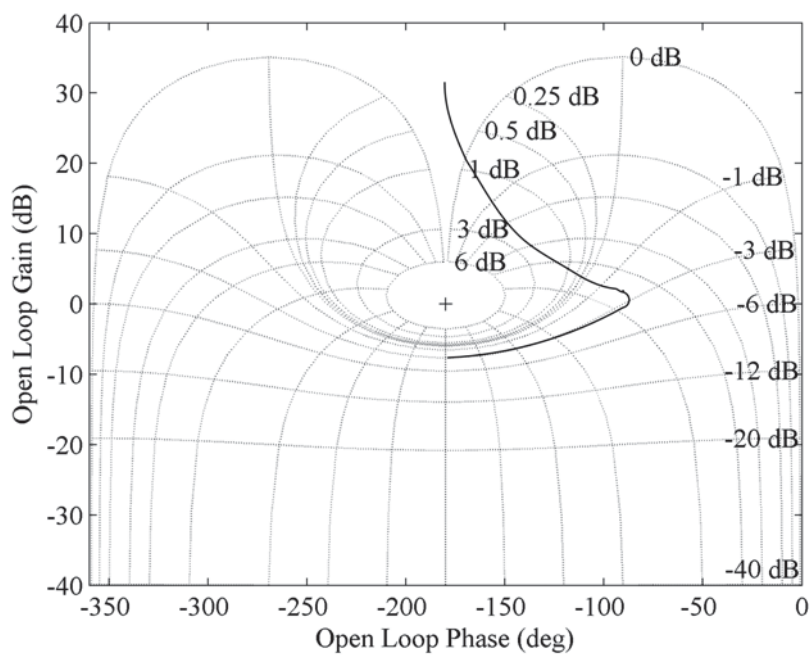


Figure 10: Typical frequency response of the closed loop altitude system

3 Hardware

This chapter describes the hardware used to acquire the data presented in Chapter 7. The airframe is first presented and then followed by the autopilot. The additional sensors are comprised of a sonar range-finder and a vision system.

3.1 Airframe

The MiniAV, shown in Figure 11, is a commercial-off-the-shelf fixed-wing airplane (Flatana, Great Planes) which has a 0.91 m wing span. The test vehicle has an all-up-weight of 410 g. The propulsion system consists of a RIMFIRE 26-28-1000kV brushless motor coupled to a 25 A electronic speed controller and a 10x3.8" propeller. The aerodynamic surfaces are controlled with micro servos.



Figure 11: Flatana from Great Planes

3.2 Autopilot

The autopilot is a Kestrel 2.2 from Procerus (see Figure 12). The onboard sensor suite is comprised of:

- 3 single-axes rate-gyros;
- 2 dual-axis accelerometers;
- 1 absolute pressure sensor;

- 1 differential pressure sensor and;
- 2 single-axis magnetometers;

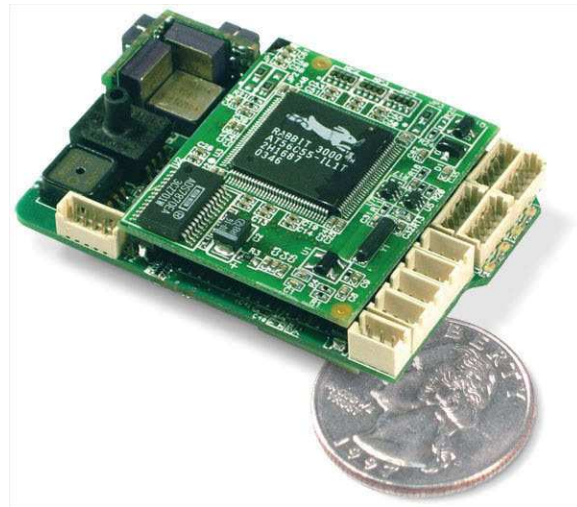


Figure 12: Procerus Kestrel 2.22 (www.procerusuav.com)

The total weight of the autopilot with a 900 Mhz Maxstream modem (XT09-MI) is of 40 grams. To communicate with the autopilot, a communication box is used (see Figure 13).



Figure 13: Communication box (www.procerusuav.com)

3.3 Additional Sensors

Additional sensors were used to complete those available on the Kestrel autopilot. For instance, to measure altitude in near to earth conditions, pressure sensors are not reliable. As a first attempt to solve the altitude measurement problem, sonar range-finders were tested. It is recognized that these devices are dependent on the absorption properties of the exposed surface, the sonar inclination and the distance between the sonar and the exposed surface.

3.3.1 Vision System

The vision system is based on the Optitrack infrared cameras from NaturalPoint (<http://www.naturalpoint.com>). The NaturalPoint Tracking Tools was used to record the markers on the MiniAV in 3D space. The reference frame of the vision system is fixed during the calibration with a calibration square (ground plane). The reference frame definition is shown in Figure 14. It was found that on the calibration square, a Z axes appears in white and that the orientation of this Z axis is in the opposite direction expected when using Tracking Tools. This error comes from an earlier version of Tracking Tools called RigidBody Toolkit that used the left hand convention.

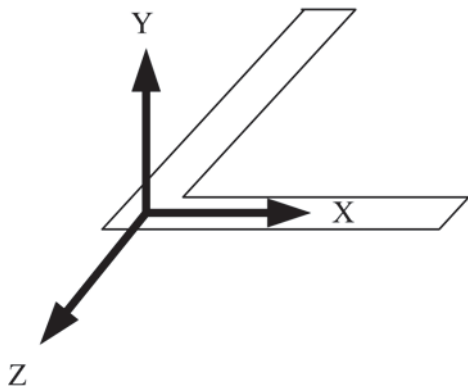


Figure 14: Vision reference frame relative to the calibration square

3.3.2 Sonar Range-Finder

Three sonar range-finders from Maxbotix were tested :

- MaxSonar EZ0;
- MaxSonar EZ2 and;
- MaxSonar EZ4.

They all have the same physical size, as illustrated in Figure 15.



Figure 15: Maxbotix MaxSonar EZ serie (www.maxbotix.com)

The main difference between the different models is their level of sensitivity to detect small objects. The associated beam patterns for each of the sensors are illustrated in Figure 16. From this figure, it is possible to observe that the Maxbotix EZ0 and EZ4 are, respectively, the most and the least sensitive of the tested sonars. Figure 16 shows the size of the beam pattern.

LV-MaxSonar®-EZ beam patterns	EZ0™	EZ1™	EZ2™	EZ3™	EZ4™
Detection pattern to a 1/8 inch diameter dowel.					
Detection pattern to a 1/4 inch diameter dowel.					
Detection pattern to a 1 inch diameter dowel.					
Detection pattern to a 3 1/4 inch diameter dowel. -5V •3.3V V+ supply voltage. (Distances overlaid on a 1 foot grid.)					

Figure 16: Beam paterns of the MaxSonar EZ serie (www.maxbotix.com)

In order to insure that all three sonar range-finders have a similar response and respect the manufacturer specifications, each sensor was tested. The measured response of the MaxSonar EZ0, EZ2 and EZ4 are illustrated in Figures 17, 18 and 19, respectively. It is possible to see from the regression linear functions that the sensitivity of the three sensors are very similar.

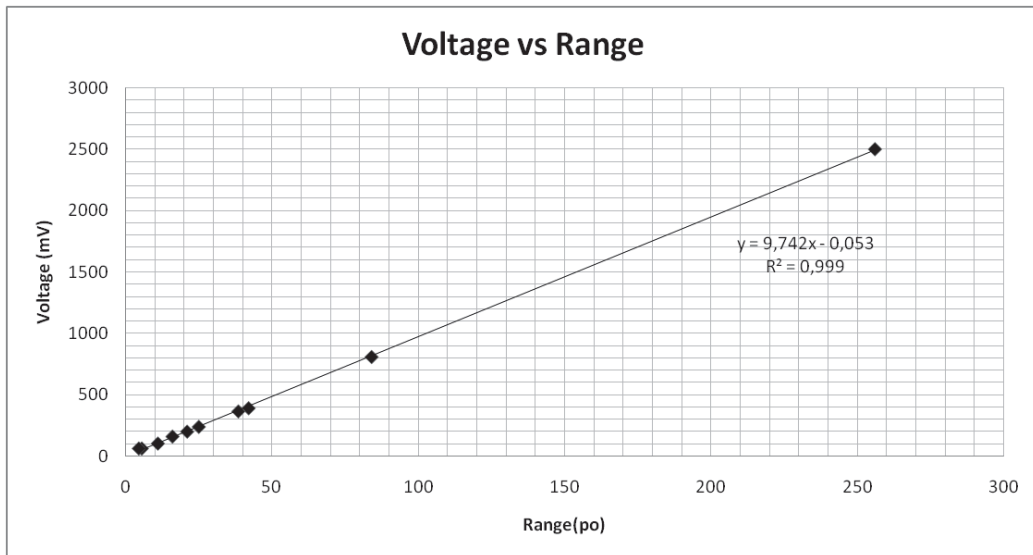


Figure 17: Response of the range-finder MaxSonar EZ0

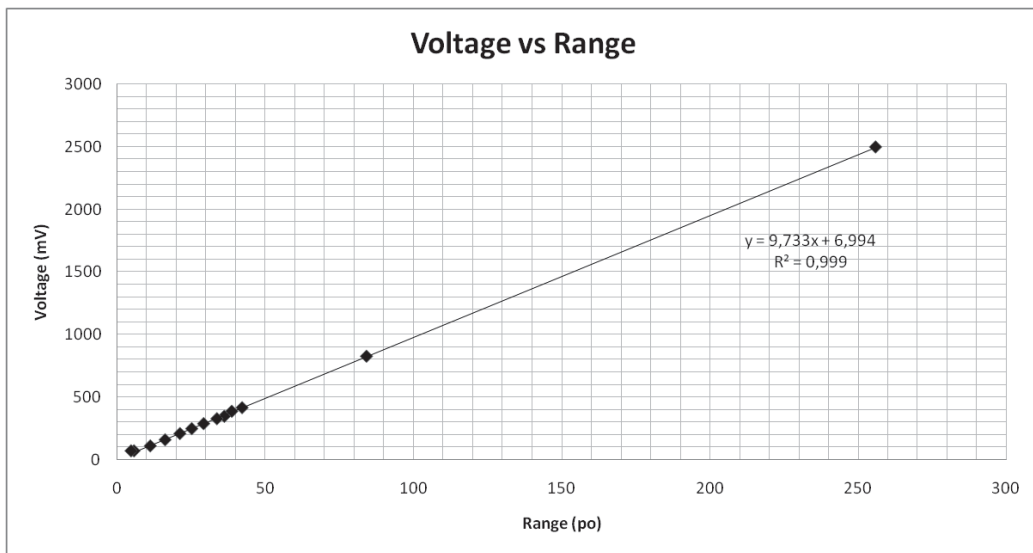


Figure 18: Response of the range-finder MaxSonar EZ2

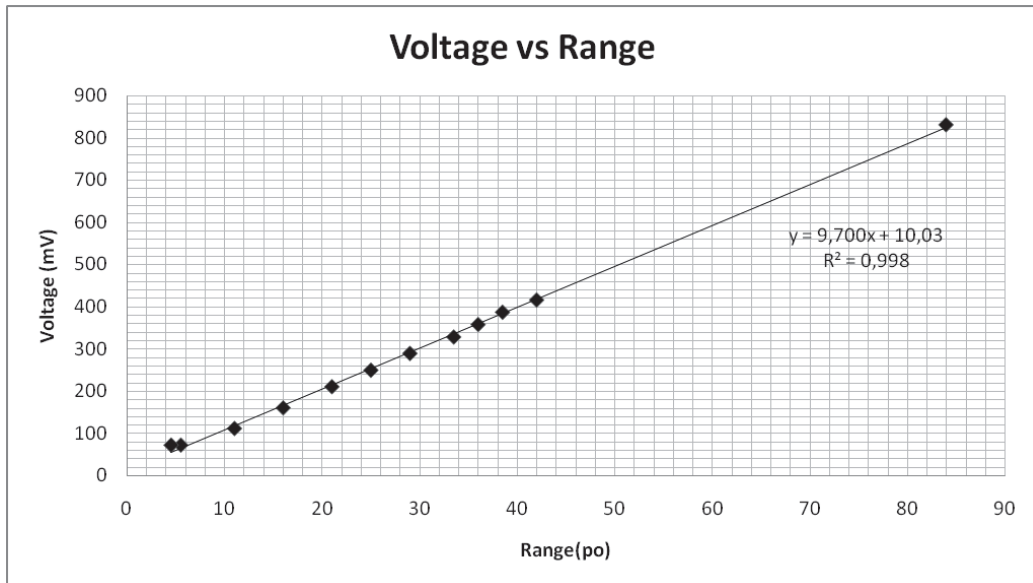


Figure 19: Response of the range-finder MaxSonar EZ4

Because the main goal of this application is to control the aircraft altitude in both outdoor and indoor conditions, tests were made over a variety of surfaces to verify the sensitivity of the three sensors. Table 4 summarizes the observations acquired during these tests. From Table 4, it is clear that for an outdoor application, the EZ0

Table 4: Outside characteristics of the tested sonar range-finders

Sensor	Grass floor	Rock and dust floor	Hard floor	6.5 m distance
MaxSonar EZ0	Very good	Very good	Very good	Very good
MaxSonar EZ2	Fair	Fair	Very good	Very good
MaxSonar EZ4	0 detection	Unstable readings	Very good	Unstable readings

is the most suited sensor because it is the least sensitive to the texture of the exposed surface. Also, it can detect a surface as far away as 6.5 meters which is the maximum rating of these sensors.

A further test was carried out where the motor was activated as measurements were made. Figure 20 illustrates the comparison between the signals measured by the sonar and by the vision system. The measurements of both systems were subtracted by their initial value to allow the comparison. Also, an offset equal to the sonar lower deadzone value (0.15 meter) was added to the sonar output because the initial conditions were setting it at less than 0.15 meters from the ground. The comparison shows that the output of the sonar generally follows the actual altitude measurements.

The sonar measurements are not entirely reliable because dropouts must be filtered adequately before using it for control. Apart from the presence of this noise, the sonar range-finder can be used to give an altitude estimation for near earth conditions.

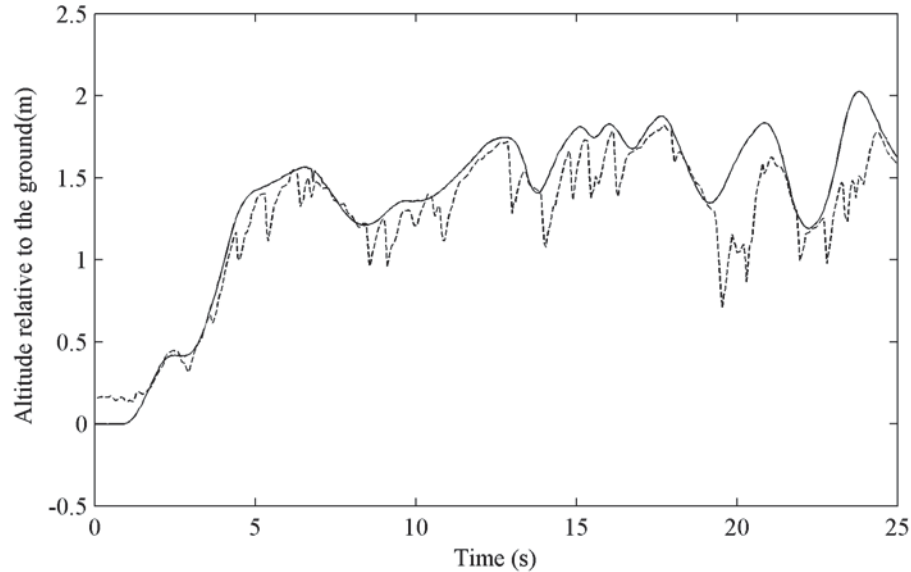


Figure 20: Comparison between the sonar and the vision system outputs

4 Sensor Data Filtering

This section presents the implementation, tuning and results obtained with the complementary filter discussed in Section 2.3.

4.1 Attitude Filter Algorithm Implementation

The calculation order of the complementary filter equations is:

1. Initialize the quaternion with an heading of 0° and with a roll and a pitch angles calculated with the normalized accelerometers readings. ($\theta = \arcsin(a_x)$ and $\phi = -a_y/\cos(\theta)$);
2. Calculate the confidence gain k_1 according to the unnormalized accelerometers readings;
3. Estimate the actual accelerometer readings with the past update of the estimated quaternion;
4. Calculate the innovation vector ω ;
5. Update the new rate-gyros bias with the calculated ω (Forward Euler integration);
6. Correct the rate-gyros readings with the estimated bias and innovation vectors;
7. Update the quaternion with the corrected rate-gyros readings (Forward Euler integration);
8. Normalize the quaternion;
9. Return to step 2.

4.2 Tuning

It is possible to specify k_p^o and k_i^o by fixing ζ which is the damping ratio and ω_0 which is the cutoff frequency of the filter.

For this application, ζ and ω_0 were adjusted by comparison with the experimental dataset to give acceptable filter performance. The values of ζ and ω_0 were set to 2 and 0.1 r/s, respectively. The confidence gain k_1 and $k_{penalty}$ were set to 1.0 and 100.0, respectively.

4.3 Comparison of the Filter Outputs with a Vision System

To examine the performance of the tuned complementary filter, its attitude estimates are compared with the attitudes measured by the absolute and drift-free vision sys-

tem. The results are illustrated in Figure 21. Apart from the presence of a drift in the roll output which is normal because of the absence of flux-magnetometers, the results are excellent for the hovering mode.

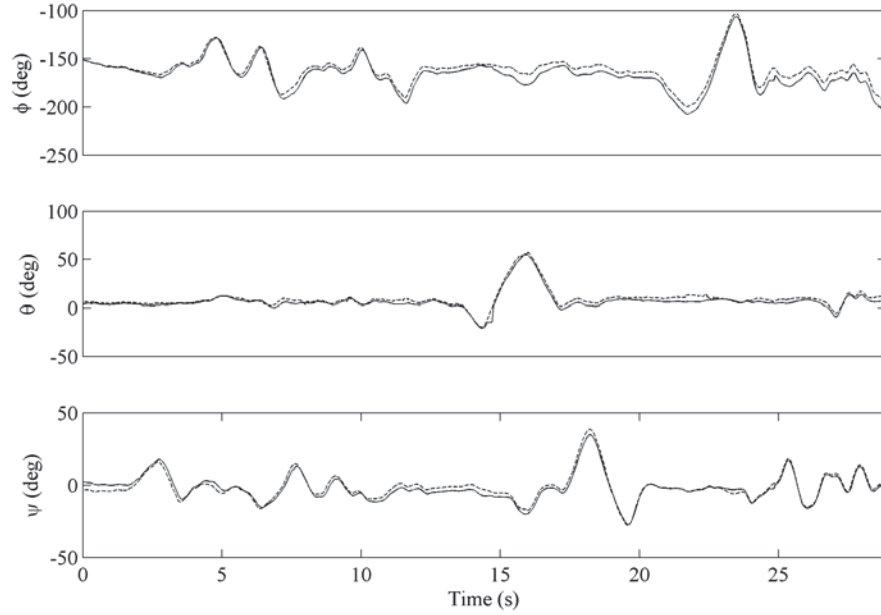


Figure 21: Comparison between the outputs of the attitude estimator without magnetometers and of a vision system : – fusion, — vision

5 Aircraft Model Identification

5.0.1 Attitude Model

The aircraft attitude model that used an offboard controller was previously identified in Bilodeau (2009). Since the weight distribution of the aircraft and the moment of inertia of the current MiniAV is very similar to the one previously studied, no additional identification testing and analysis was conducted. The only difference between model used in the previous study and this study is time delay present in the systems. Because all calculations and measurements are done onboard with the Kestrel autopilot instead of being relayed to an offboard controller, the measured time delay was reduced from 0.17 s to 0.05 s.

With the new time delay of 0.05 s, the attitude models are

$$\frac{p(s)}{\delta_{ailerons}(s)} \left(\frac{\text{rad/s}}{\text{ms}} \right) = \frac{-10.55e^{-0.05s}}{0.67s + 1} = \frac{-s\phi(s)}{\delta_{ailerons}(s)} \quad (15)$$

$$\frac{q(s)}{\delta_{elevator}(s)} \left(\frac{\text{rad/s}}{\text{ms}} \right) = \frac{-4.827se^{-0.05s}}{(1.67s - 1)(0.06s + 1)} = \frac{-s\theta(s)}{\delta_{elevator}(s)} \quad (16)$$

$$\frac{r(s)}{\delta_{rudder}(s)} \left(\frac{\text{rad/s}}{\text{ms}} \right) = \frac{7.79se^{-0.05s}}{(1.43s - 1)(0.12s + 1)} = \frac{-s\psi(s)}{\delta_{rudder}(s)} \quad (17)$$

5.0.2 Altitude Model

Experimental observations and modeling show that the inputs $\delta_{ailerons}$ and $\delta_{throttle}$ are both coupled to the altitude output h . The main coupling is between $\delta_{throttle}$ and h . This coupling was identified with a predictive error method found in the process identification tool from the Matlab system identification toolbox. A sampling time of 0.05 s was used. A two steps approach was employed. First, the throttle was actioned in open loop with large excitations. A linear time-invariant model was identified assuming small perturbations around a selected operating point and then validated through comparison with experimental data. The fit for the identification and validation dataset are illustrated in Figures 22 and 23. The residuals are presented in Figure 24. Because the identified model is capable of capturing the main dynamics of the validation data output and because the residuals resemble white noise, it was concluded that the open loop model was satisfactory. No attempt was made to resolve the time-varying offset error observed in Figure 23 at this point. This question is re-visited in Sec. 6.2.

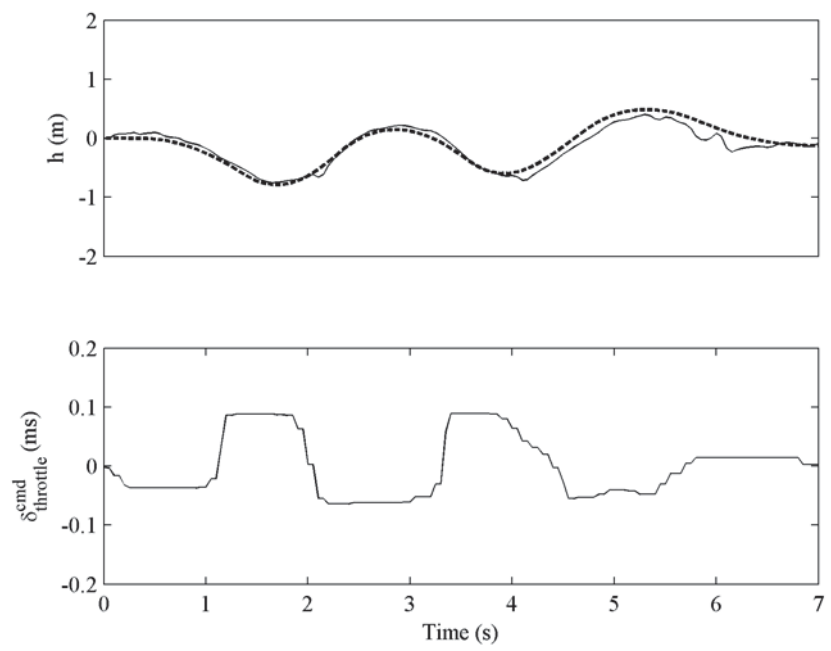


Figure 22: Fit for the open loop identification of the coupling between $\delta_{throttle}$ and the altitude. Dashed line - fit. Solid - measured. Relative to operation points.

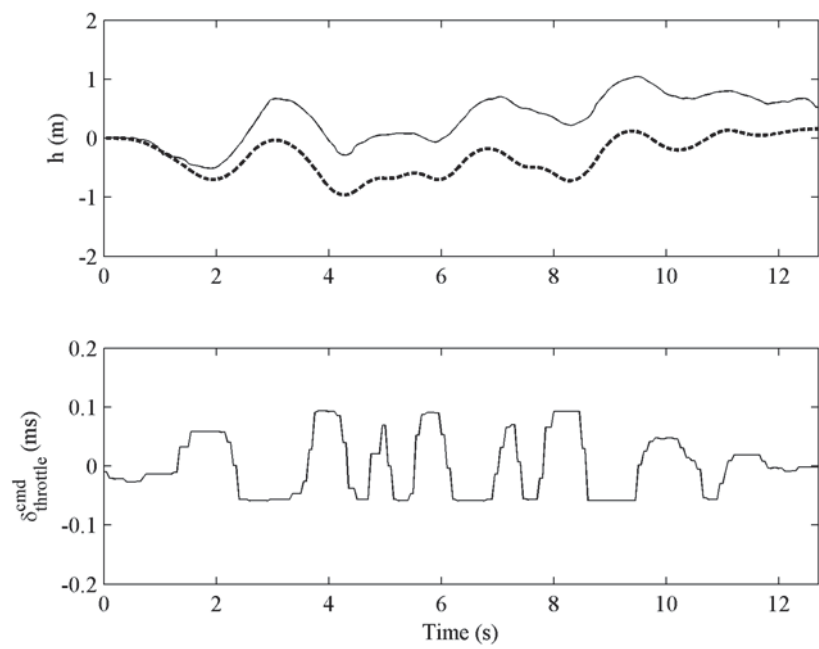


Figure 23: Validation fit for the open loop identification of the coupling between $\delta_{throttle}$ and the altitude. Dashed line - fit. Solid - measured. Relative to operation points.

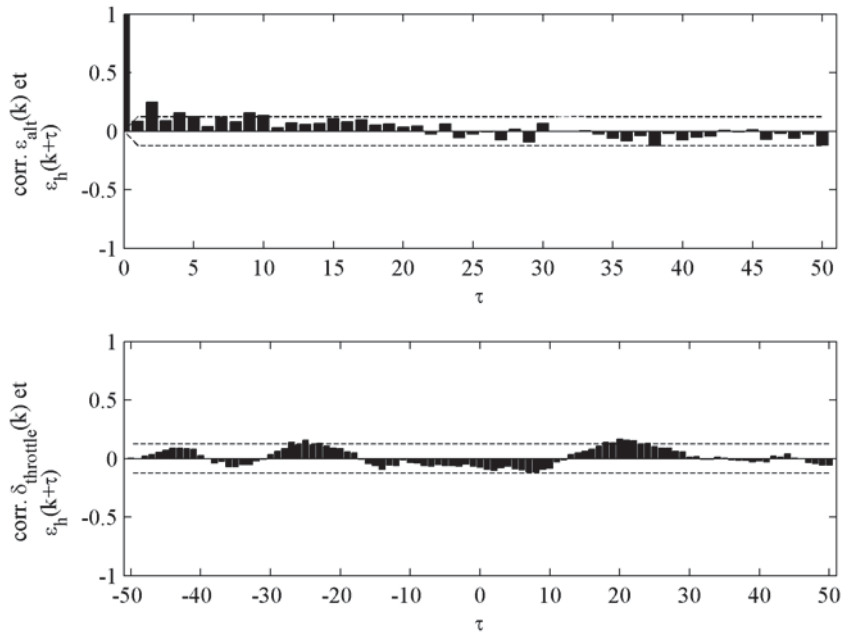


Figure 24: Autocorrelation of residuals for the coupling between the altitude and $\delta_{throttle}$

With the main open loop altitude/throttle coupling transfer function identified, a Proportional-Integral-Derivative (PID) controller and decoupler (Subsection 2.6.2) were designed to close the loop between the throttle and altitude without considering the cross-coupling with the ailerons. With the throttle/altitude controller in place, a second identification test was carried out where the ailerons were actioned by sending rapid setpoint changes to the roll controller.

Figures 25 and 26 present the fit for the identification and validation datasets while Figure 27 presents the residuals. It can be seen that the fit is excellent and that the residuals resemble white noise.

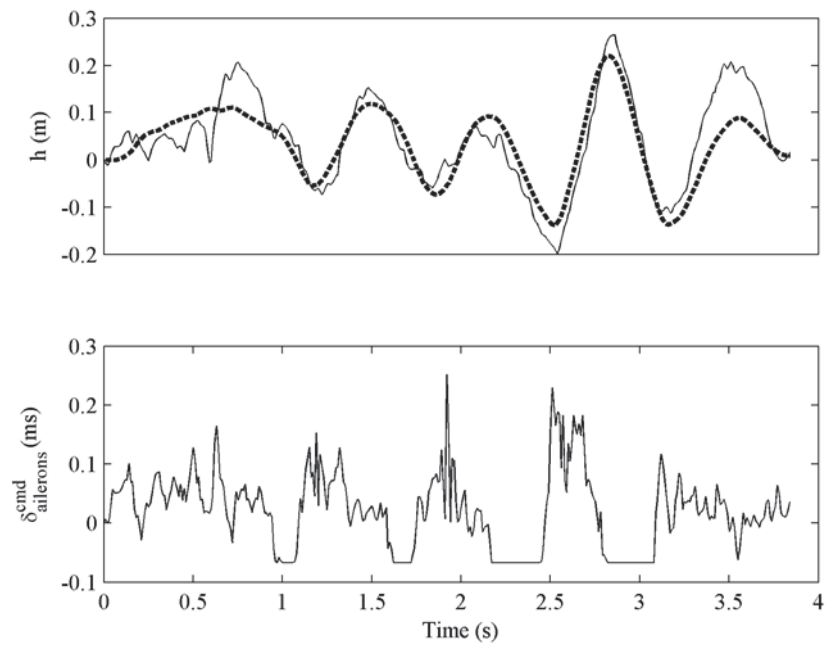


Figure 25: Fit for the open loop identification of the coupling between δ_{ailerons} and the altitude. Dashed line - fit. Solid - measured. Relative to operation points.

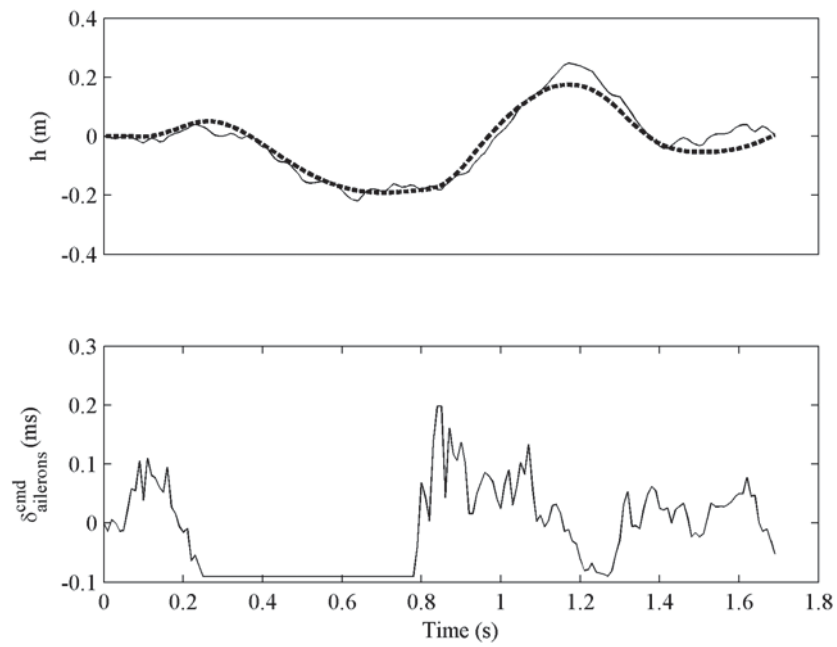


Figure 26: Validation fit for the open loop identification of the coupling between δ_{ailerons} and the altitude. Dashed line - fit. Solid - measured. Relative to operation points.

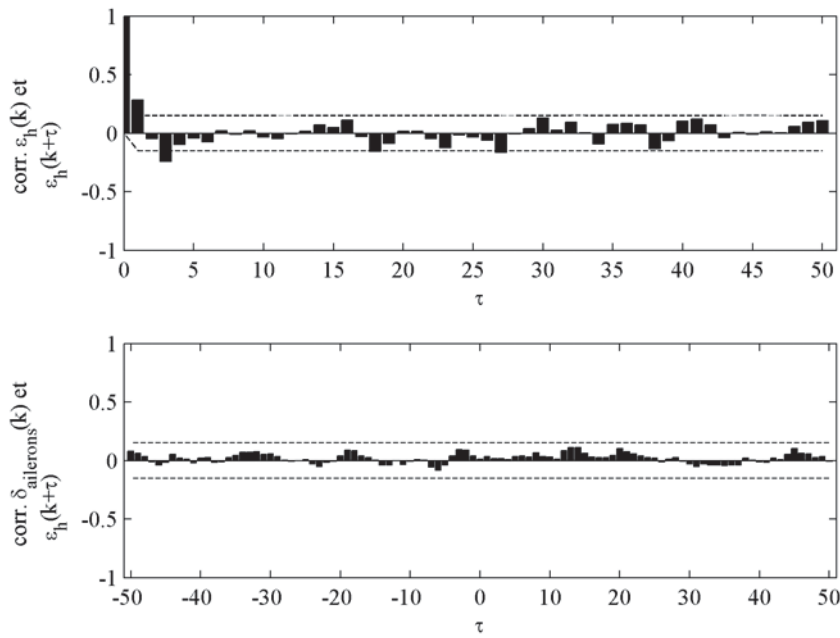


Figure 27: Autocorrelation of residuals for the coupling between the altitude and δ_{ailerons}

Table 5 presents the identified transfer functions that are valid for the experimental characterisation conditions. The altitude output is expressed in the continuous time domain.

Table 5: Identified transfer functions for the altitude

	δ_{ailerons} (ms)	δ_{throttle} (ms)
$h(m)$	$\frac{1.52e^{-0.05s}}{s(0.22s+1)}$	$\frac{23.97e^{-0.20s}}{s(0.3s+1)}$

6 Control Tuning

This chapter presents the calculated and implemented gains for the attitude and altitude controllers. It also details the frequency responses and the ailerons to altitude decoupler design.

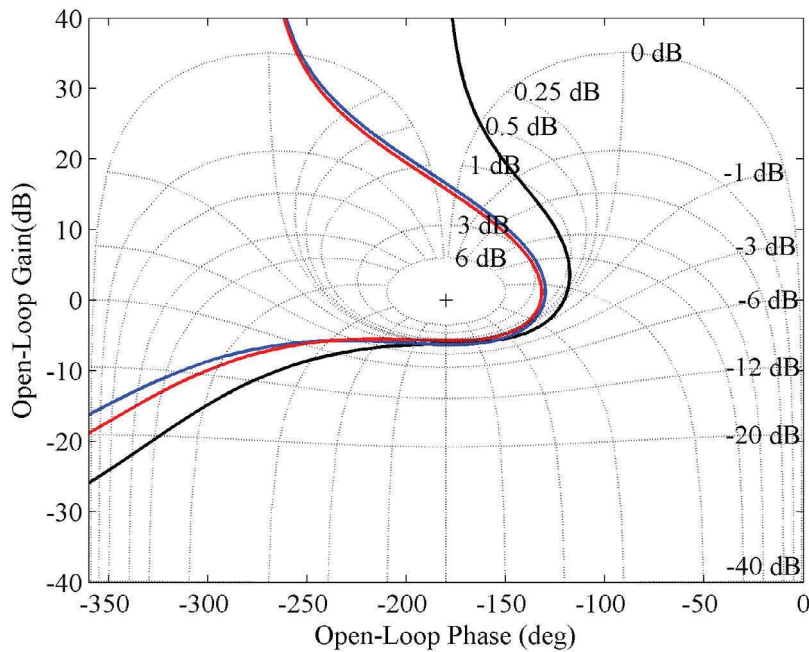
6.1 Attitude Control Tuning

Table 6 presents the calculated and implemented tunings. The internal gain of the pitch controller was increased from -0.23 to -0.30 to reduce the low frequency oscillations.

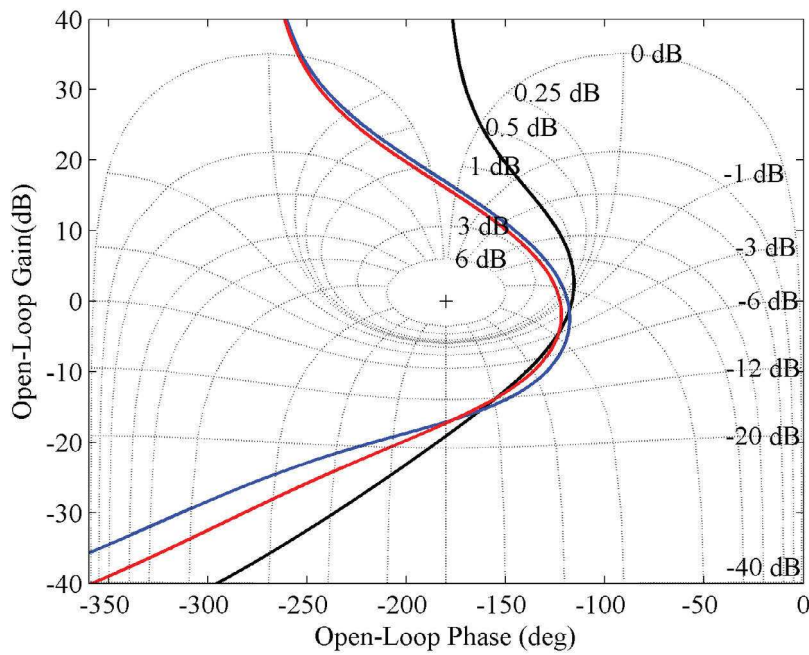
Table 6: Controller parameters

Controller	Tuning	$K_c(\frac{rad/s}{rad})$	$T_i(s)$	$K_i(\frac{ms}{rad/s})$
Calculated	Roll	2.5	3	-0.35
	Pitch	6.0	2	-0.23
	Yaw	5.5	2	0.17
Implemented	Roll	2.5	3	-0.35
	Pitch	6.0	2	-0.30
	Yaw	5.5	2	0.18

To illustrate the benefits obtained with lower time delays, open loop frequency responses of the external loops are generated with two different time delays. Based on these calculated gains and on the models given by equations 15 to 17, Figure 28 illustrates the frequency responses obtained with a time delay of 0.17 s and 0.05 s. The associated properties of the closed system are presented in Table 7. From this table and Figure 28, it is clear that an important increase in gain margin is obtained. The increased gain margin allows a greater model gain uncertainty to be present. In practical terms, the larger margin will result in reduced vehicle oscillations in the presence of perturbations or in transient modes. The theoretical reason is simple, with a time delay of 0.17 s, increasing the gain will make the frequency response cross the lower section of the high dB contours resulting in an oscillating behavior at higher frequency. However, with the time delay of 0.05 s, the gain increase must be bigger to create the same behavior. This mean that a lower time delay results in a more robust controller for a same adjustment of the controller parameters.



(a) Time delay of 0.17 s



(b) Time delay of 0.05 s

Figure 28: Frequency response of the attitude controllers with different time delays

Table 7: Property of the closed loop system with the 0.17 s and 0.05 s time delay

Controller	ω_{co} (rad/s)	ω_{180} (rad/s)	ω_b (rad/s)	M_r (dB)	ϕ_m (deg)	A_m (dB)
Delay (s)	0.17	0.05	0.17	0.05	0.17	0.05
Roll	2.07	1.93	6.60	7.49	4.53	5.56
Pitch	2.82	2.66	9.09	20.53	6.27	17.87
Yaw	2.68	2.49	8.09	16.50	5.41	14.00
				3	2.8	47.61
						57.32
						5.70
						17.25

6.2 Altitude/Throttle Control Tuning

The tuning of the altitude controller is done with the main coupling transfer functions given in Table 5. The resulting PID transfer function is expressed by

$$G_h(s) = \frac{0.025(2s+1)(1.8s+1)}{2s(0.01s+1)} \quad (18)$$

and the resulting frequency response is illustrated in Figure 29.

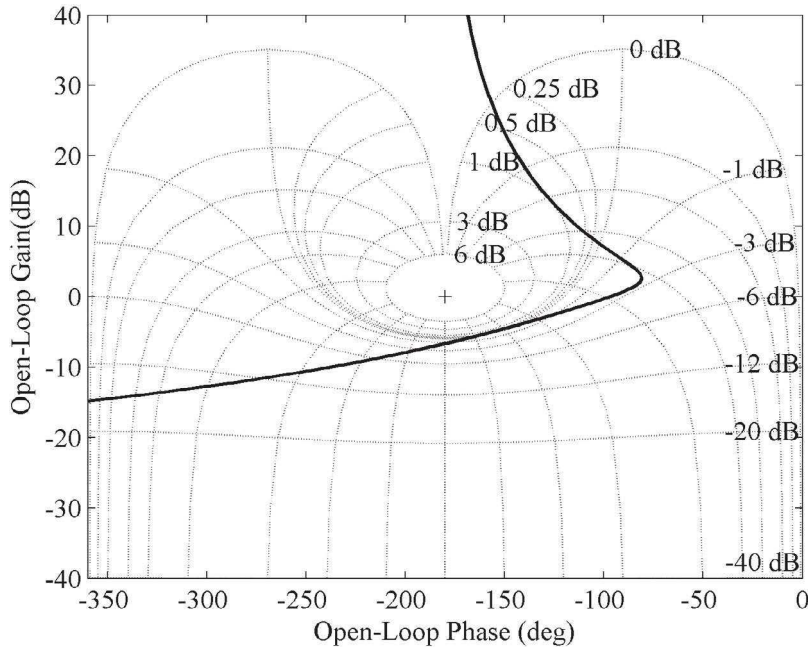


Figure 29: Frequency response of the altitude controller

The anticipation transfer function was calculated using transfer functions from Table 5. The ideal decoupler, omitting the time delay, can be found as follows

$$D = -\frac{G_{aileron}}{G_{throttle}} = -\frac{0.0634(0.3s+1)}{e^{-0.15s}(0.22s+1)} \approx -\frac{0.0634(0.3s+1)}{(0.22s+1)} \quad (19)$$

To reduce the complexity and the impact of an eventual identification error, a static gain is preferred to the decoupler in eq. 19 because it is a phase advance. The equivalent static gain is -0.1 . Figure 30 illustrates the step response of the cross-coupling between $\delta_{ailerons}$ and h with and without the anticipation. As illustrated in this figure, the static gain can perform as well as the nominal anticipation transfer function within a time window when altitude setpoint changes normally occur.

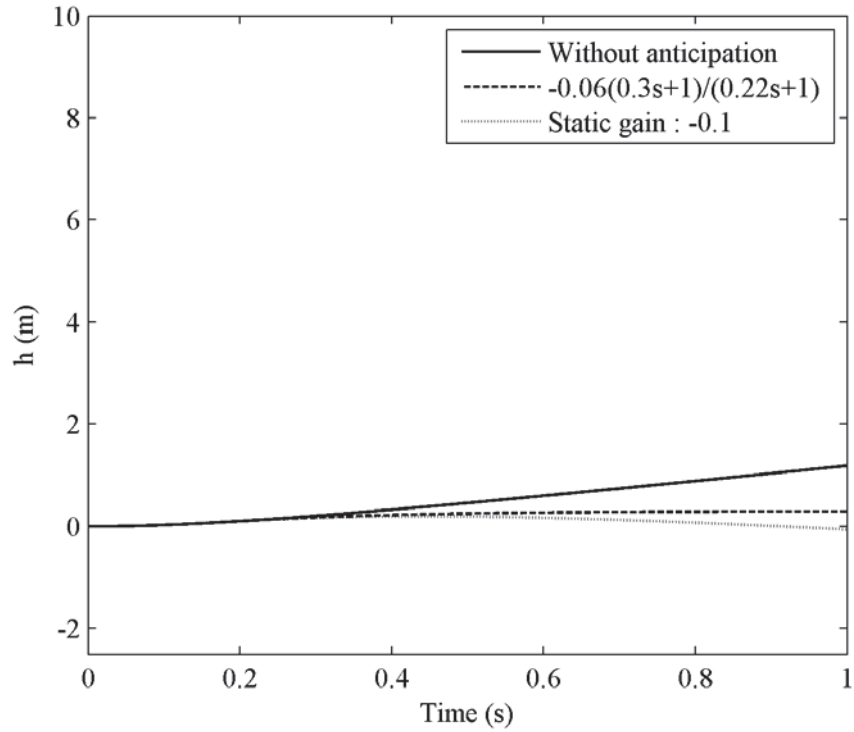


Figure 30: Step response of the coupling between $\delta_{ailerons}$ and h

7 Experimental Validation of the Tuned Controllers

Experimental results obtained with the controllers described in Section 2.5 are presented. The measured and desired quaternions were converted to vertical Euler representation (ϕ , θ and ψ) for convenience.

7.1 Attitude Control Results

Figures 31 to 34 illustrate results obtained with the implemented controller parameters given in Table 6. For the outputs ϕ , θ and ψ , a dotted line representing $\pm 3^\circ$ performance bounds is added around the setpoints. The $\pm 3^\circ$ bound was selected as a reasonable target for the evaluation of control performance. It is worth noting that $\delta_{throttle}^{trim}$ is equal to 1.0 and not the true trim value in hover for implementation reasons.

Figure 31 illustrates the results obtained when the air vehicle is maintained in hovering mode with negligible commands given by the operator. Between 5 and 8 seconds of the flight test, the vehicle is pitched back to bring the vehicle closer to the operator. From 8 to 32 s, no operator inputs are given. After ~ 32 s, some correction on the pitch and yaw commands are done. In these conditions, the attitude is well controlled. Note that, in the first 10 s, the vehicle is stabilizing from its manual launch, therefore the observed roll error is expected. This error eventually disappears after 10 s.

Figure 32 illustrates results where the vehicle is in hovering mode and the roll setpoint is changed constantly to assess the performance of the roll controller and verify the interaction between the ailerons and the other controllers. The results show that the pitch and yaw controllers do not react in concert to the changes in the aileron deflections. The main maneuvering limitation of the hovering fixed wings can be observed in the results. To counteract the propeller torque, the ailerons have to operate close maximum deflection permitted by the aileron servo. The lack of additional aileron deflection, after the propeller torque has been countered, causes the observed roll errors. Saturation of the ailerons is observed when the command reaches -0.2 ms.

Figure 33 illustrates the results for lateral translations commanded by changing the yaw setpoint. In this test, the pitch was adjusted to position the vehicle in a safe attitude before executing the translations. It can be seen that the heading, which corresponds to the roll angle, changes over time. This drift is caused by the lack of a heading sensor that feeds data to the attitude estimator. The error observed on the yaw angle is caused by inputting yaw setpoint changes faster than the lateral dynamics of the air vehicle allows. With slower setpoint changes, the yaw controller is capable of following the setpoints easily. The conclusions of this test are that the

vehicle tracks the behavior in lateral translation with no coupling observed between the controllers in this kind of maneuver.

Figure 34 illustrates the results where all the setpoints are changed to move the vehicle randomly in space. The objective of this test is to prove the repeatability of the controllers in variable conditions. The performance of the pitch and yaw controllers is still excellent. However, the saturation of the ailerons still generates error in roll.

Globally, the results obtained for the angles θ and ψ in Figures 31 to 34 are better than those obtained by Bilodeau (2009). The onboard control system has less time delay, resulting in increased stability margins and better dynamic performance. Another contributor to the improved performance can be attributed to increased structural stiffness of the airframe used in the experiments. It was observed that if the airframe has a weakness between the empennage and the fuselage where the inertial sensors are installed, the structural vibrations generated by this weakness will be read as angular oscillations by the sensors. Appropriate structural reinforcement eliminated this problem. The results obtained for the angle ϕ are in general very well regulated. However, the torque generated by the propeller may be too high for the roll control available in this platform design. A counter-rotating propeller unit may be a solution to reduce the torque.

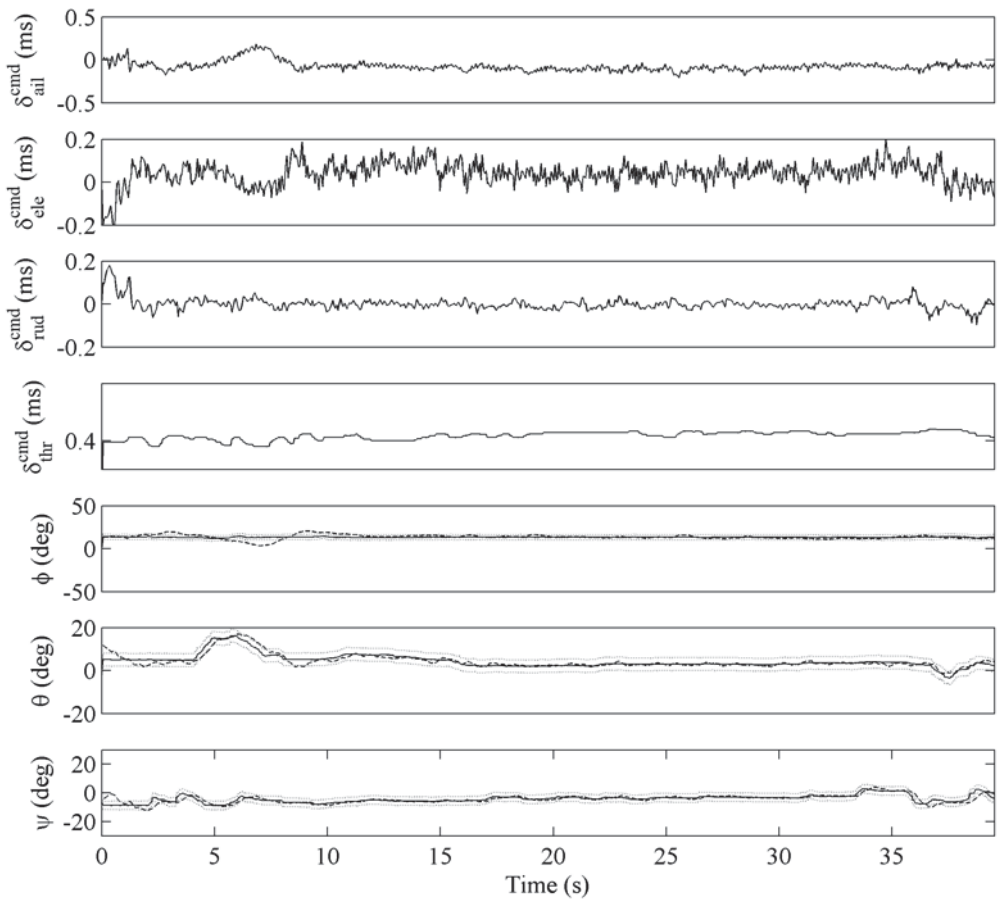


Figure 31: Flight results #1 obtained with the Flatana

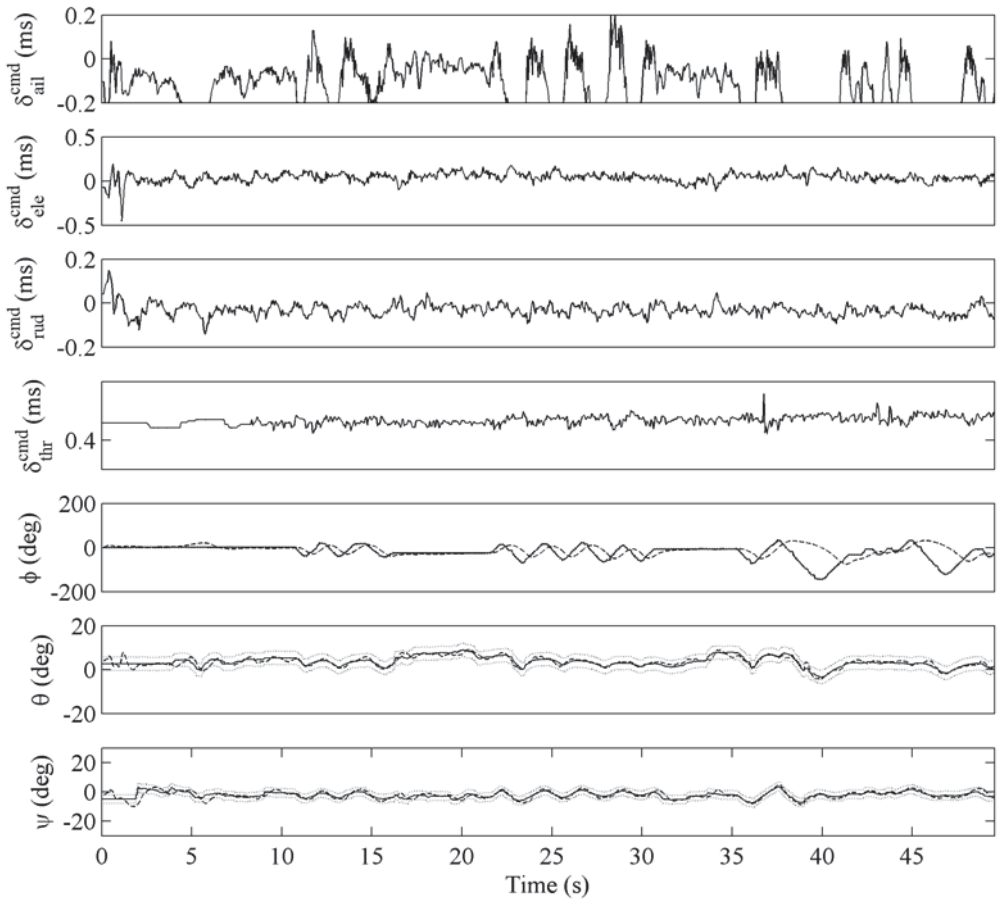


Figure 32: Flight results #2 obtained with the Flatana

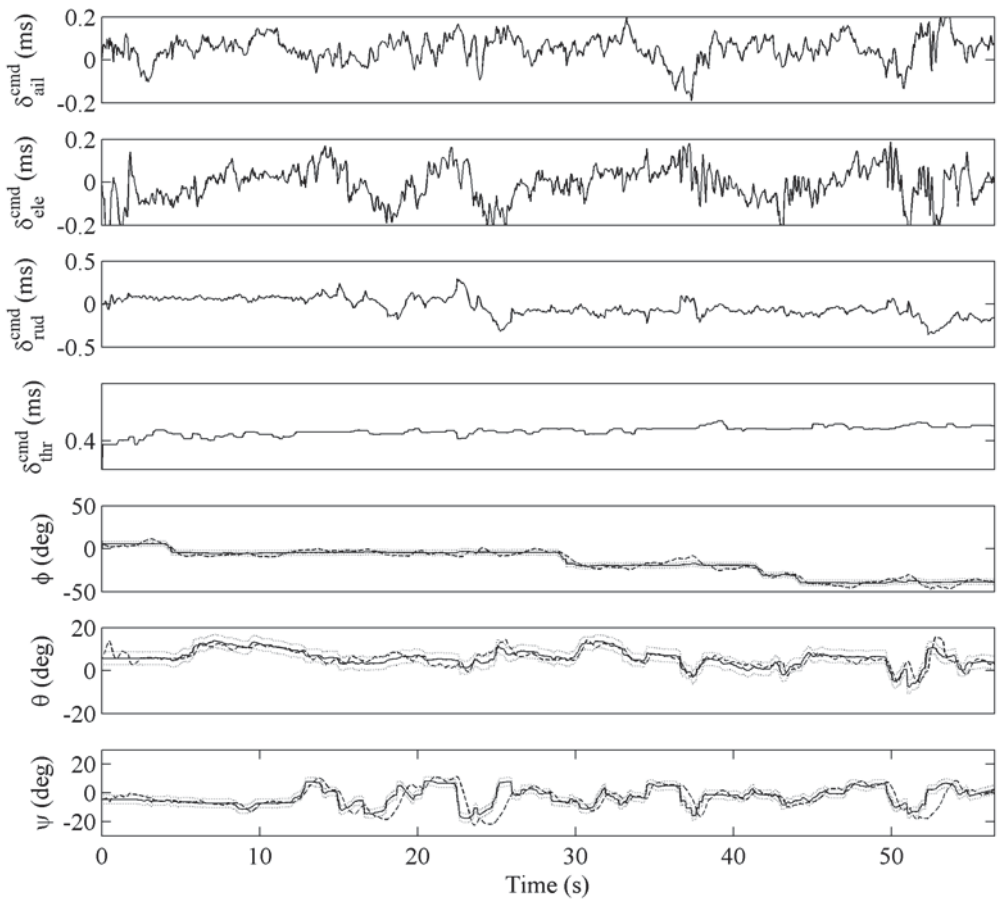


Figure 33: Flight results #3 obtained with the Flatana

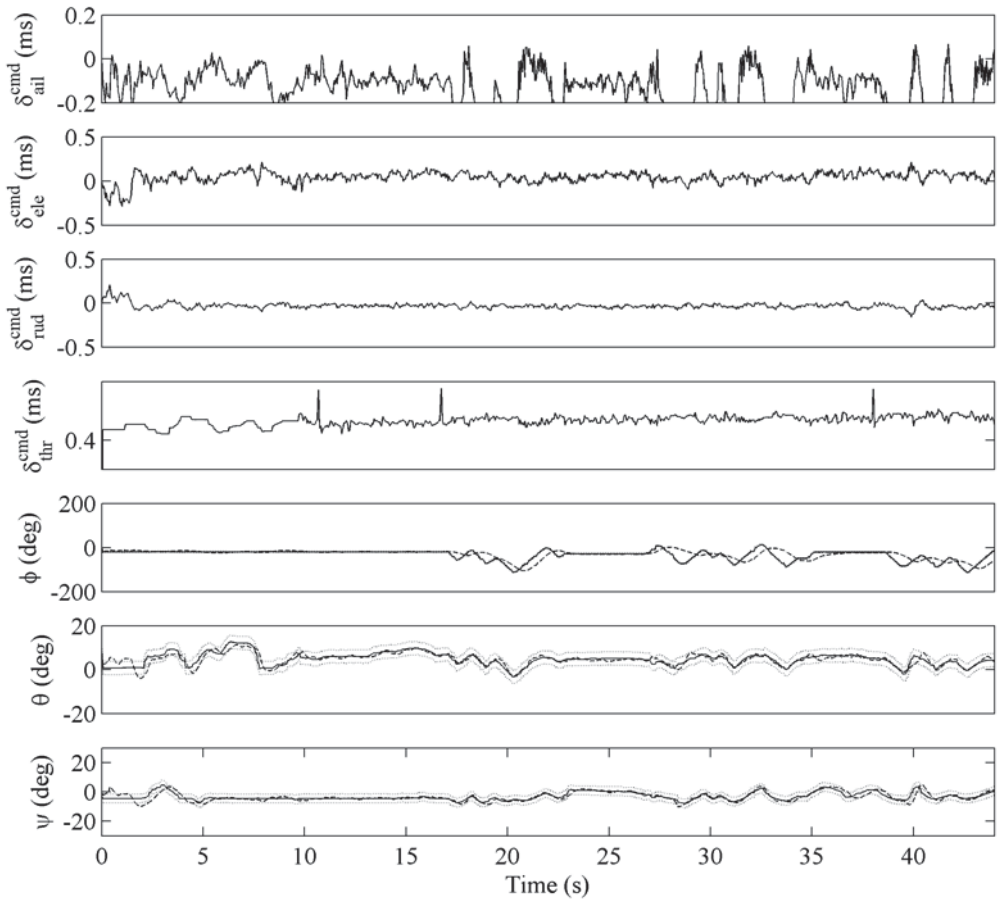


Figure 34: Flight results #4 obtained with the Flatana

7.2 Altitude/Throttle Stabilization Results

Tests on the altitude/throttle controller were carried out with and without the anticipation transfer function (Subsection 2.6.2) activated to see what the gain in performance would be. The results obtained with the anticipation function deactivated are illustrated in Figure 35. It can be seen that the ailerons generate perturbations on the altitude. Figure 35 shows that all perturbations fall within a ± 25 cm bound around the setpoint. Figure 36 shows the altitude/throttle control with the anticipation function activated. The ailerons saturate to the same extent as the previous test, except the perturbations now all fall within a ± 10 cm bound. These results clearly demonstrate the benefits of the roll-throttle decoupler.

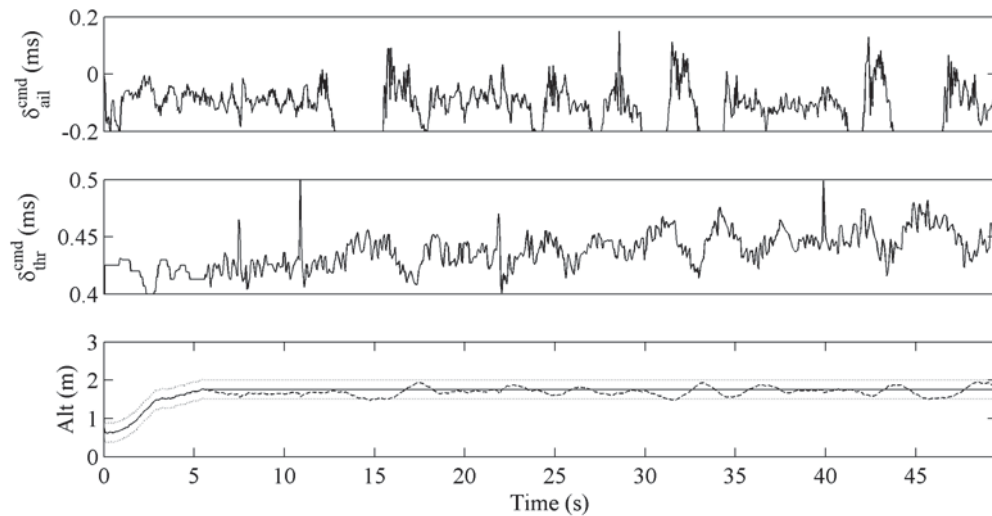


Figure 35: Flight results with altitude controller : ± 0.25 cm bounds

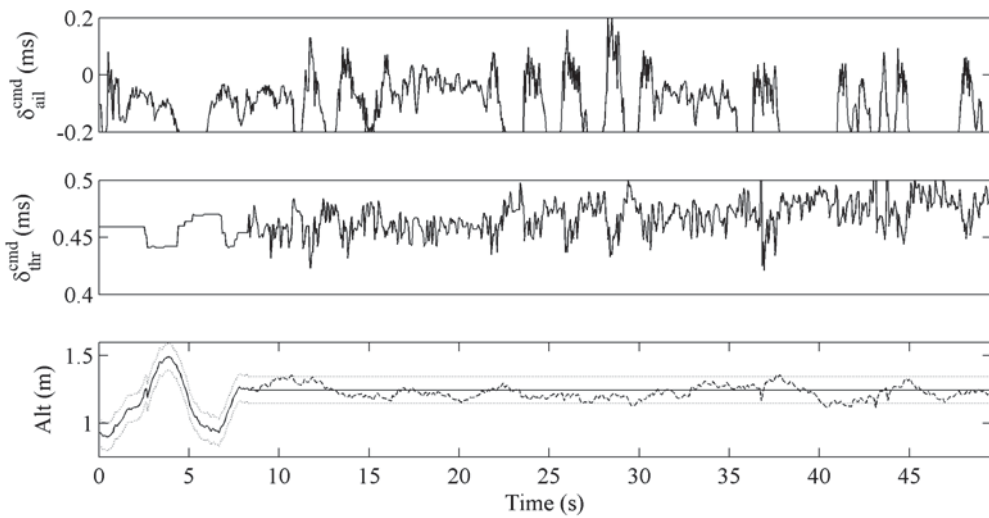


Figure 36: Flight results with altitude controller and static decoupler : ± 0.10 cm bounds

7.3 Effect of the Throttle on the Roll Controller

The effect of throttle changes on the roll controller is investigated. To better observe the response of the roll controller, the anticipation transfer function (Subsection 2.6.2) was de-activated.

Figure 37 illustrates the results of the test. The test was achieved by trying to keep the altitude constant while modulating the throttle manually. It can be seen in the ϕ results that the perturbations induced by the throttle changes are very well damped. Some overshoots occur around 15 s because the ailerons are momentarily saturated. This behaviour is also observed between 27 and 35 s. Based on these results, it was concluded that a decoupler for the roll controller to cancel out the effect of the throttle was unnecessary.

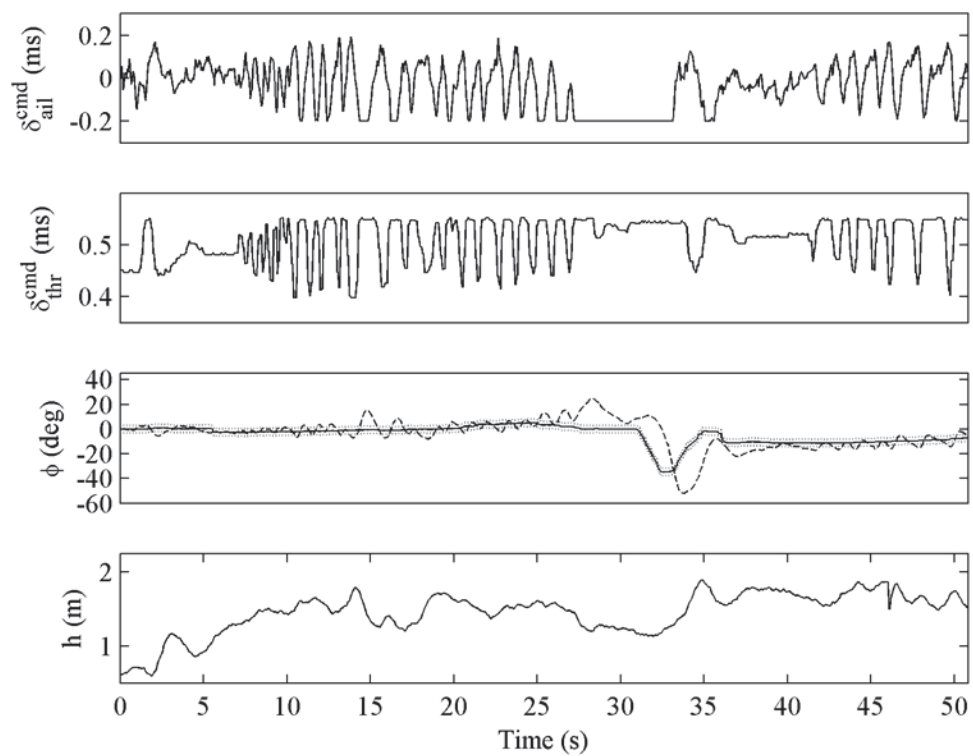


Figure 37: Flight results #3 - Effect of throttle variation on the roll controller

8 Conclusions

The theoretical basis for measuring the attitude and altitude, and stabilizing a mini-aerial vehicle while being flown in a hovering position was presented. A cascaded PI control architecture based on quaternion attitude measurements and a PID altitude/throttle controller with anticipation due to aileron perturbations were formulated and implemented on an onboard autopilot. A complementary filter was employed to improve the stability and reliability of the attitude measurements that fed the controllers. Tuning of the attitude and altitude/throttle control gains was first accomplished on a calibrated dynamic 6DOF airplane model using a frequency response method to meet the desired performance goals. The calculated gains did not change significantly when implemented in the test vehicle, indicating that the airplane model dynamics were equivalent. The implementation of the controllers on the onboard autopilot reduced previous system delays from 0.17 s to 0.05 s. The result was a significant increase in the amplitude margin from roughly 6 to 17 dB in the pitch and yaw axes. This increase in margin allows the controller to handle greater model gain uncertainties and to better reduce oscillations if the vehicle is perturbed from its equilibrium position. The experimental data showed that throttle commands, compensated for aileron effects through an anticipation function, reduced the altitude hold error from ± 25 cm to ± 10 cm, thereby validating the necessity of a roll-throttle decoupler to stably hover an aircraft of this type at a fixed altitude.

9 Recommendations

A control architecture based on classical proportional-integral-derivative techniques was developed for a platform with a standard fixed wing configuration to enable it to hover stably in ideal conditions. Future work should address the following items:

- Employment of nonlinear parameter identification to better capture the behavior of a hovering fixed wing platform beyond the localized set point conditions.
- Development of a six degree of freedom flight dynamics model that better captures the nonlinear behavior of a hovering fixed wing platform.
- Investigation and comparison of other control methods to evaluate their effectiveness and their computational demands.
- Investigation of the ability of the platform and control scheme to compensate for exogenous disturbances.
- Investigation of other platform planforms and control surface configurations.

References

- Ahmadi, M., Khayatian, A., and Karimaghaei, P. (2007), Orientation Estimation by Error-State Extended Kalman Filter in Quaternion Vector Space, *SICE Annual Conference*.
- Bachmann, E. R., Yun, Xiaoping, and Brumfield, A. (2007), Limitations of Attitude Estimation Algorithms for Inertial/Magnetic Sensor Modules, *IEEE Robotic and Automation Magazine*.
- Bilodeau, P.-R. (2009), Commande d'un mini véhicule aérien sans pilote en vol stationnaire pour l'opération en milieu restreint, Master's thesis, Université Laval.
- DeBlauwe, H., Bayraktar, S., Feron, E., and Lokumcu, F. (2007), Flight Modeling and Experimental Autonomous Hover control of a Fixed Wing Mini-UAV at High Angle of Attack, *AIAA GNC*.
- Frank, A., Mcgrew, J., Valenti, M., Levine, D., and How, J.P. (2007), Hover, Transition, and Level Flight Control Design for a Single Propeller Indoor Airplane, Technical Report Aerospace Controls Laboratory, Department of Aeronautics and Astronautics.
- Green, W.E. (2007), A Multimodal Micro Air Vehicle for Autonomous Flight in Near-Earth Environments, Ph.D. thesis, Drexel University.
- Green, W.E. and Oh, P.Y. (2005), A MAV That Flies Like an airplane and Hovers Like a Helicopter, *International Conference on Advanced Intelligent Mechatronics*, pp. 694–698.
- Green, W.E. and Oh, P.Y. (2006), Autonomous Hovering of a Fixed-Wing Micro Air Vehicle, *IEEE International Conference on Robotics and Automation*, pp. 2164–2169.
- Green, W.E. and Oh, P.Y. (2006), A Fixed-Wing Aircraft for Hovering in Caves, Tunnels, and Buildings, *American Control Conference*, pp. 1092–1097.
- Hamel, T. and Mahony, R. (2006), Attitude estimation on $\text{SO}(3)$ based on direct inertial measurements, *ICRA2006*.
- Knoebel, N. (2007), Adaptative Quaternion Control Of a Miniature Tailsitter UAV, Master's thesis, Brigham Young University.
- Knoebel, N., Osborne, S., Snyder, D., McLain, T.W., Beard, R., and Eldredge, A. (2006), Preliminary Modeling, Control, and trajectory Design for miniature Autonomous tailsitters, *AIAA GNC*.

- Knoebel, N. B. and Mc Lain, T.W. (2008), Adaptative Quaternion Control of a Miniature Tailsitter UAV, *American Control Conference*.
- Kuipers, J.B. (1999), Quaternions and Rotation Sequences, Princeton University Press.
- Mahony, R., Cha, S.-H., and Hamel, T. (2006), A coupled estimation and control analysis for attitude stabilisation of mini aerial vehicles, *Australasian Conference on Robotics and Automation*.
- Maxbotix, <http://www.maxbotix.com/MaxbotixHome.html>.
- Metni, N., Pflimlin, J.-M.l, Hamel, T., and Souères, P. (2006), Attitude and gyro bias estimation for a VTOL UAV, *Control Engineering Practice*, 14, 1511–1520.
- Mueller, Thomas J. and al. (2007), Introduction to the Design of Fixed-Wing Micro Air Vehicles, AIAA Education series.
- Phillips, W.F. (2004), Mechanics of Flight, Wiley.
- Phillips, W.F., Hailey, C.E., and Gebert, G.A. (2001), Review of Attitude Representations Used for Aircraft Kinematics, *Journal of Aircraft*, 38(4).
- Pomerleau, A. and Poulin, E. (1996), PID Tuning Methods for Integrating and Unstable Processes, *IEE proc. D*, 143(5), 429–435.
- Poulin, E. and Pomerleau, A. (1996), PID Tuning Methods for Integrating and Unstable Processes, *IEE proc. D*, 143(5), 429–435.
- Stone, R.H. (2004), Control Architecture for a Tail-Sitter Unmanned Air Vehicle, *5th Asian Control Conference*, 2, 736–744.
- Yun, X. and Bachmann, E.R. (2006), Design, Implementation, and Experimental Results of a Quaternion-Based Kalman Filter for Human Body Motion Tracking, *IEEE Transactions on Robotics*, 22(6).

Annex A: User Guide

Before executing a flight demonstration, it is necessary to have the following items :

- A computer capable of running DevDemo.exe (provided on the CD);
- A Kestrel communication box connected to the serial port 5 of the computer;
- An air vehicle with the Kestrel autopilot mounted onboard;
- A joystick as illustrated in figure A.1; and
- Fully charged 2- and 3-cell lithium-polymer batteries.

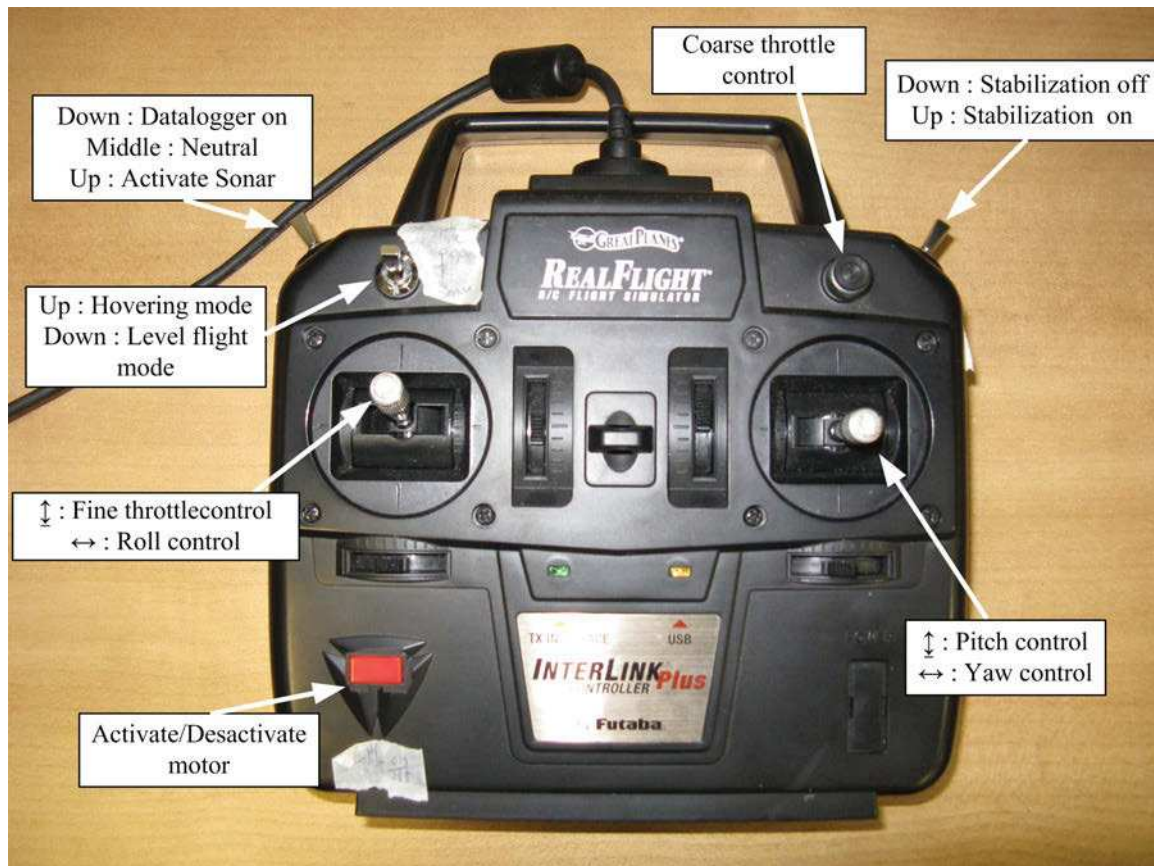


Figure A.1: Joystick and switch configurations on the controller handset

To execute the demo, follow the following step :

1. Verify that the communication box is connected to the communication (COM) port 5 of the computer;
2. Verify that the controller handset is connected to any USB port of the computer and that the switches are in a safe state (stabilization off, sonar loop not enabled, and hovering mode);
3. Power on the communication box;

4. Place the air vehicle horizontally on the ground;
5. Plug the 2-cell lithium-polymer battery to the autopilot power connector;
6. Open the application DevDemo.exe, an interface as illustrated in Figure A.2 should appear;
7. Click on the "Open port" button;
 - If the port has opened, the "Open port" button will disable itself;
 - Otherwise, verify the communication box is connected to COM5;
8. If a datalog is desired, first specify the duration and the sampling rate in the textbox contained in "Datalog" button group. Then the datalog can be started manually with the "StartDatalog" button or automatically at the flight test beginning by setting the joystick tristate switch to the "Datalogger on" position;
9. The PID controller parameters can be modified with the text boxes contained in the "Cascade Loop Tuning" group;
 - Two controller modes are available, the level flight mode and the hovering mode, these controllers can be chosen by checking or not the checkbox located under the "GetDefaultValues" button which is used to retrieve default values.
 - To download the PID parameters values to the autopilot, click on the "SetFlashValues" button;
 - To retrieve the PID parameters values in the autopilot, click on the "Get-PIDValues" button;
10. To verify that the attitude estimator is not giving false estimations, a blue triangle is drawn in the 3D environment. The longest side of the triangle indicates the right side of the vehicle;
11. Plug the 3-cell lithium-polymer battery to the ESC power connector;
12. Lift and hold the aircraft in a vertical attitude (nose pointing up);
13. Press the red button (motor activation) on the controller handset;
14. Start the motor by activating stabilization (stabilization switch on), put the fine throttle control at $\frac{1}{2}$ travel and adjust coarse throttle control in a position where the aircraft can lift itself;
15. Switch off the stabilization (stabilization switch off) to reset the controllers and to ensure a proper takeoff;
16. Place the aircraft vertically before the take off sequence;
 - Manually control the rate of ascent for vertical take-off with the throttle (the orientation will be stabilized);
 - When the desired altitude is reached, activate the sonar loop which will automatically hold the airplane at constant altitude;
17. To land, de-activate the sonar loop and manually control the altitude with the throttle until the airplane has landed;
18. When the vehicle has landed, turn off the stabilization (stabilization switch off).

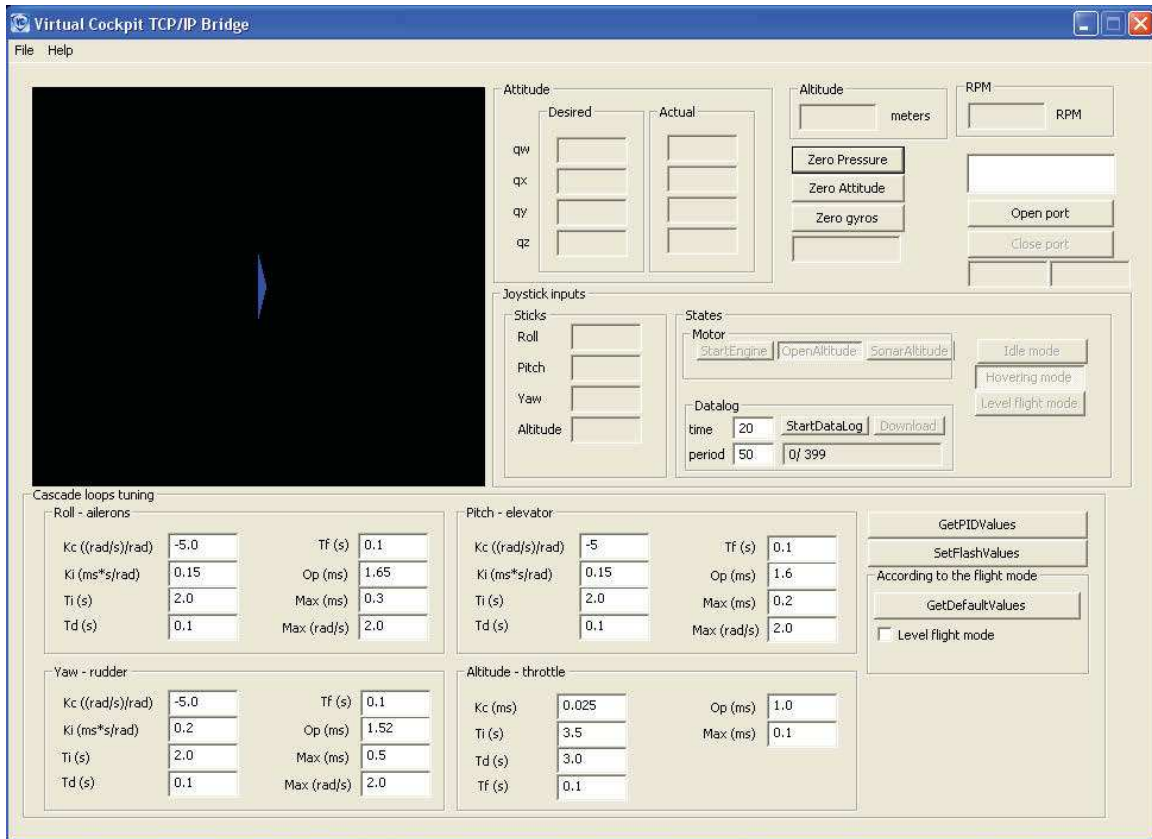


Figure A.2: Interface built for study

UNCLASSIFIED
SECURITY CLASSIFICATION OF FORM
(Highest Classification of Title, Abstract, Keywords)

DOCUMENT CONTROL DATA		
1. ORIGINATOR (name and address) Defense R&D Canada - Valcartier 2459 boul. Pie XI North Quebec, QC, G3J 1X5	2. SECURITY CLASSIFICATION (Including special warning terms if applicable) UNCLASSIFIED	
3. TITLE (Its classification should be indicated by the appropriate abbreviation (S, C, R or U)) Extreme Agility Micro Aerial Vehicle - Control of hovering maneuvers for a mini-aerial vehicle with an onboard autopilot system		
4. AUTHORS (Last name, first name, middle initial. If military, show rank, e.g. Doe, Maj. John E.) Bilodeau, P-R., Wong, F.		
5. DATE OF PUBLICATION (month and year) February 2011	6a. NO. OF PAGES 53	6b .NO. OF REFERENCES 24
7. DESCRIPTIVE NOTES (the category of the document, e.g. technical report, technical note or memorandum. Give the inclusive dates when a specific reporting period is covered.) Technical Report		
8. SPONSORING ACTIVITY (name and address)		
9a. PROJECT OR GRANT NO. (Please specify whether project or grant) 12pn01	9b. CONTRACT NO.	
10a. ORIGINATOR'S DOCUMENT NUMBER TR 2010-144	10b. OTHER DOCUMENT NOS N/A	
11. DOCUMENT AVAILABILITY (any limitations on further dissemination of the document, other than those imposed by security classification) <input checked="" type="checkbox"/> Unlimited distribution <input type="checkbox"/> Restricted to contractors in approved countries (specify) <input type="checkbox"/> Restricted to Canadian contractors (with need-to-know) <input type="checkbox"/> Restricted to Government (with need-to-know) <input type="checkbox"/> Restricted to Defense departments <input type="checkbox"/> Others		
12. DOCUMENT ANNOUNCEMENT (any limitation to the bibliographic announcement of this document. This will normally correspond to the Document Availability (11). However, where further distribution (beyond the audience specified in 11) is possible, a wider announcement audience may be selected.) Unlimited		

UNCLASSIFIED
SECURITY CLASSIFICATION OF FORM
(Highest Classification of Title, Abstract, Keywords)

UNCLASSIFIED
SECURITY CLASSIFICATION OF FORM
(Highest Classification of Title, Abstract, Keywords)

13. ABSTRACT (a brief and factual summary of the document. It may also appear elsewhere in the body of the document itself. It is highly desirable that the abstract of classified documents be unclassified. Each paragraph of the abstract shall begin with an indication of the security classification of the information in the paragraph (unless the document itself is unclassified) represented as (S), (C), (R), or (U). It is not necessary to include here abstracts in both official languages unless the text is bilingual).

Mini Aerial Vehicles (MiniAV) are involved in various unmanned missions for both civil and military applications. These airplanes benefit from high maneuverability and can generally execute hovering and other acrobatic maneuvers. The small size of these vehicles, combined with their high maneuverability, have inspired numerous research studies in which these vehicles are envisioned for use in missions involving hazardous locations or situations in which human lives are at risk. The theoretical basis for measuring the attitude and altitude, and stabilizing a mini-aerial vehicle while being flown in a hovering position is presented. A cascaded PI control architecture based on quaternion attitude measurements and a PID altitude/throttle controller with anticipation due to aileron perturbations were formulated and implemented on an onboard autopilot. The implementation of the controllers on the onboard autopilot reduced previous system delays from 0.17s to 0.05s. The result was a significant increase in the amplitude margin from roughly 6 to 17dB in the pitch and yaw axes. The experimental data showed that throttle commands, compensated for aileron effects through an anticipation function, reduced the altitude hold error from +/- 25cm to +/- 10cm, thereby validating the necessity of a roll-throttle decoupler to stably hover an aircraft of this type at a fixed altitude.

14. KEYWORDS, DESCRIPTORS or IDENTIFIERS (technically meaningful terms or short phrases that characterize a document and could be helpful in cataloguing the document. They should be selected so that no security classification is required. Identifiers, such as equipment model designation, trade name, military project code name, geographic location may also be included. If possible keywords should be selected from a published thesaurus, e.g. Thesaurus of Engineering and Scientific Terms (TEST) and that thesaurus-identified. If it is not possible to select indexing terms which are Unclassified, the classification of each should be indicated as with the title.)

PID, autopilot, MAV, hovering, complementary filter, quaternion, sonar, range finder, identification

UNCLASSIFIED
SECURITY CLASSIFICATION OF FORM
(Highest Classification of Title, Abstract, Keywords)

Defence R&D Canada

Canada's Leader in Defence
and National Security
Science and Technology

R & D pour la défense Canada

Chef de file au Canada en matière
de science et de technologie pour
la défense et la sécurité nationale



www.drdc-rddc.gc.ca

